Materials Chemistry and Physics 277 (2022) 125526

Contents lists available at ScienceDirect

Materials Chemistry and Physics

journal homepage: www.elsevier.com/locate/matchemphys

Temperature dependent structural, dielectric, Raman, piezoresponse and photoluminescence investigations in sol-gel derived BCZT ceramics

Indrani Coondoo [a,*], Alexander Krylov [b], Dhananjay K. Sharma [c,1], Svetlana Krylova [b], Denis Alikin [a,d], J. Suresh Kumar [e], A. Mirzorakhimov [d], Nina Melnikova [d], Manuel J. Soares [e], Andrei L. Kholkin [a,d,f]

[a] Department of Physics & CICECO – Aveiro Institute of Materials, University of Aveiro, 3810-193, Aveiro, Portugal
[b] Laboratory of Molecular Spectroscopy, Kirensky Institute of Physics, Federal Research Center KSC SB RAS, Krasnoyarsk, 660036, Russia
[c] DEMaC & CICECO – Aveiro Institute of Materials, University of Aveiro, 3810-193, Aveiro, Portugal
[d] School of Natural Sciences and Mathematics, Ural Federal University, 620026, Ekaterinburg, Russia
[e] I3N-Aveiro, Department of Physics, University of Aveiro, 3810-193, Aveiro, Portugal
[f] Physical Materials Science and Composite Materials Centre, Research School of Chemistry & Applied Biomedical Sciences, National Research Tomsk Polytechnic University, Tomsk, 634050, Russia

HIGHLIGHTS

- Detailed analysis of Raman spectroscopy over a wide temperature range reveal the phase sequence as: R(R3c).→R(R3m)→O→T→C
- The R3c .→ R3m transition observed near −175 °C has never been reported earlier in sol-gel derived BCZT.
- Temperature-dependent PFM studies reported for first time in sol-gel derived BCZT ceramics.
- PFM investigation revealed a complex domain pattern with nanoscale blotchy domains having blurry domain boundaries.
- PL studies indicated the existence of localized states in the band gap that allow emission in visible spectral region.

ARTICLE INFO

Keywords:
Lead-free piezoelectrics
Sol-gel
Phase transitions
Raman spectroscopy
PFM
Photoluminescence

ABSTRACT

$0.5Ba(Ti_{0.8}Zr_{0.2})O_3$-$0.5(Ba_{0.7}Ca_{0.3})TiO_3$ [50BZT-50BCT or BCZT] based compounds have been the focus of a lot of research, particularly motivated by their high piezoelectric effect. However, the literature lacks an elaborate investigation of the phase transition behavior in BCZT ceramics obtained by wet chemistry processing. Here, we present an in-depth study on the temperature dependence of x-ray diffraction (XRD), Raman scattering, dielectric properties, local piezoresponse and photoluminescence (PL) to investigate the sequence of phase transitions in the BCZT ceramic synthesized *via* a chemical route. Phase formation was determined by Rietveld analysis of XRD data, while compositional homogeneity and elemental quantification of the compound was validated using energy dispersive x-ray spectroscopy (EDX) and x-ray photoelectron spectroscopy (XPS) studies. Detailed fitting of XPS data indicated the existence of Ti^{3+} species (~6%) in the prepared BCZT. Phase transitions were examined by analyzing the modifications in the XRD profile of Bragg reflection {200} and anomalies observed in the temperature variation of dielectric and Raman spectra studied over a wide temperature range starting from 10K to beyond Curie temperature. Crystallographic transformation temperatures obtained from dielectric measurement agreed well with those assessed from the temperature evolution of Raman spectra. In addition to other transitions, Raman scattering results revealed the existence of a transition from *R3c* to *R3m* phase near −175 °C, a transition that has not been interpreted in BCZT (and generally not observed in parent $BaTiO_3$ compound). The luminescence response was studied by photoluminescence (PL) spectroscopy in the temperature range 15–300 K. The position of the PL peak was observed to shift with temperature and discontinuities in the wavelength shift were noted near phase transitions. Evolution of domain morphology with temperature was examined by

* Corresponding author.
E-mail address: indrani.coondoo@ua.pt (I. Coondoo).
[1] Current affiliation: Institute of Physics of the Czech Academy of Sciences, Cukrovarnicka 10, 16200 Prague, Czech Republic.

https://doi.org/10.1016/j.matchemphys.2021.125526
Received 17 April 2021; Received in revised form 11 August 2021; Accepted 4 December 2021
Available online 8 December 2021

piezoresponse force microscopy technique. Consolidated results assign the phase sequence in sol-gel derived BCZT as: $R\,(R3c) \xrightarrow{-175\pm10\,^{\circ}C} R\,(R3m) \xrightarrow{-50\pm10\,^{\circ}C} O \xrightarrow{40\pm10\,^{\circ}C} T \xrightarrow{120\pm10\,^{\circ}C} C$.

1. Introduction

Piezoelectric materials represent the core group of functional materials for sensors and actuators. The most efficient piezoelectric compounds are based on lead zirconate titanates (PZT) that exhibit exceptional piezoelectric performance (d_{33} = 220–590 pC/N), and, therefore, find a wide range of applications [1,2]. However, owing to its lead toxicity, research on lead-free materials witnessed an upsurge with the main objective of discovering materials that can suitably compete and replace the lead-containing PZT family. In this pursuit, about a decade ago, Saito *et al*. [3], reported a non-toxic alternative that spurned wide-spread scientific activity. They identified a mixture of polymorphic phase transition (PPT) and morphotropic phase boundary (MPB) region in an alkaline niobate-based composition $(K_{0.44}Na_{0.52}Li_{0.04})(Nb_{0.86}Ta_{0.10}Sb_{0.04})O_3$ having piezoelectric coefficient values comparable to PZT. The ceramic exhibited d_{33} = 300 pC/N which was further improved to d_{33} = 416 pC/N with texturing [3]. However, the major disadvantage of a KNN-based system is the requirement of elaborate synthesis conditions owing to the hygroscopic nature of the constituent oxides. Another widely studied lead-free material is the binary system $(1-x)(Bi_{0.5}Na_{0.5})TiO_3$-$xBaTiO_3$ [BNT-BT], having a MPB between the ferroelectric tetragonal and rhombohedral phases at x~0.06–0.08 [4], characterized by enhanced piezoelectric properties. Typically, the MPB composition shows an electromechanical coupling factor k_p = 52% and a d_{33} = 125 pC/N [5]. Nevertheless, among others, the $BaTiO_3$-based solid solution having the composition: $0.5Ba(Ti_{0.8}Zr_{0.2})O_3$-$0.5(Ba_{0.7}Ca_{0.3})TiO_3$ [BCZT] garnered huge attention following the remarkable piezoelectric coefficient (d_{33} = 620 pC/N) observed in bulk ceramics [6].

In the present work, comprehensive temperature-dependent studies have been undertaken to clarify the sequence of phase transitions in sol-gel-derived BCZT composition. An extensive literature survey confirms that there are previous reports on structural and temperature-dependent electrical characterization of sol-gel derived BCZT ceramics [7–15]; however, the temperature dependence was confined to above room temperature only. Detailed investigations on the sequence of phase transitions, including dielectric and Raman scattering studies over a wide temperature span (starting from as low as 10 K to nearly 670 K), on a sol-gel-derived BCZT has not been reported yet. Generally, distinct anomalies in dielectric, piezoelectric, mechanical, and thermal properties are observed at phase transitions that can be exploited in device applications; therefore, this study is important from this perspective.

BCZT bulk ceramic was prepared by a chemical route, namely, the sol-gel process which is a low-temperature synthesis method and provides high purity and composition homogeneity. Structural studies of the prepared sample were performed using x-ray diffraction (XRD) and Raman scattering methods. It is known that standard XRD measurements provide primarily the global macroscopic symmetry while identification of local symmetry of smaller cluster regions with different ferroelectric phases may not be precise. On the contrary, Raman spectroscopy characterizes lattice dynamics and local structure, thereby providing information on low symmetry ferroelectric phases and local structural distortions. An exhaustive analysis was done on the temperature behavior of Raman scattering data collected over a temperature range 8–680 K that revealed the presence of a low-temperature transition and also confirmed the existence of the intermediary orthorhombic phase. To further establish the sequence of transitions, the BCZT samples were probed by photoluminescence spectroscopy in the temperature range 15–300K. Luminescence spectra are extremely sensitive to variations in structural environment; thus, any structural change such as phase transition, can be perceived via variation in the luminescence intensity and/or wavelength shifts. Temperature behavior of domain morphology has not been reported thus far in sol-gel derived BCZT ceramics. Therefore, to understand the modifications in the domain configuration with temperature, the non-destructive nanoscale imaging technique namely piezoresponse force microscopy (PFM) was used.

2. Experimental details

BCZT bulk ceramics having composition $Ba_{0.85}Ca_{0.15}Ti_{0.9}Zr_{0.1}O_3$ were synthesized by chemical solution method (sol-gel route; hereinafter to be referred as sg-BCZT). The details of the synthesis procedure can be found in ref [**7**]. The cylindrical pellets were sintered at 1350 °C for a dwelling time of 3 h.

Surface morphology of the sample was obtained on the as-sintered surface using a Field Emission Scanning Electron Microscope (Hitachi S-4100 FESEM equipped with energy-dispersive x-ray spectroscopy EDX). Estimation of the average grain size was done using the ImageJ software. Further statistical computations were performed to assess the grain size distribution and average grain size. Elemental distribution mapping was acquired by EDX. Estimation of relative density (ratio between the apparent density and the theoretical density) was done using Archimedes' principle. Phase formation of the sintered sample was verified using an x-ray diffractometer equipped with a graphite monochromated CuK_α radiation source (Phillips X'Pert, Almelo, Netherlands). Before measurement, the sintered ceramic disc was pulverized and annealed at 400 °C for an hour to release strains. GSAS-EXPGUI software suite was utilized for Rietveld refinement on the full profile fitting of the XRD patterns. High-resolution X-ray photoelectron spectroscopy (XPS) spectra were acquired on SPECS NAP-XPS system (monochromatic AlKα (1486.74 eV) x-ray source), under an ultra-high vacuum (base pressure of 2×10^{-10} mbar). The binding energies in the XPS spectra were calibrated against the adventitious carbon C 1s singlet (binding energy, BE = 284.6 eV). The XPS data were processed using CASAXPS software.

Temperature-dependent Raman spectra were recorded in the temperature range 8–680 K, on a Horiba Jobin Yvon T64000 spectrometer with closed-cycle ARS CS204-X1.SS helium cryostat under a vacuum of 10^{-6} mBar. The temperature was tracked using LakeShore DT-6SD1.4L silicon diode with a stabilization accuracy of ~0.1K. The excitation light source used was an Ar + ion laser (Spectra-Physics Stabilite 2017) with λ = 514.5 nm. Measurements of low-wavenumber spectral edge were performed in the subtractive dispersion mode. Dielectric measurements were carried out using two set-ups (i) an LCR meter (Agilent 4284A) in the temperature range 100–400 K and (ii) a precision impedance analyser (Solartron 1260A) in temperature range 10–300K. Prior to electrical measurements, samples were polished and coated with silver paste (AGG302, Agar Scientific Ltd., UK), followed by curing at 550 °C for 30 min.

For domain morphology analysis, the sample surface was rigorously polished sequentially using diamond pastes (DP-Paste, Struers A/S, Ballerup, Denmark) having abrasive particles of size 1 μm and 1/4 μm. Thereafter, the polished samples were annealed at 400 °C in air for 2 h to ease the mechanical stress induced by polishing. Domain imaging was performed using piezoresponse force microscopy (PFM) technique on an atomic force microscope (MFP-3D, Asylum Research, Oxford Instruments, UK), equipped with a high-temperature module. The PFM signal was obtained in a DART mode at the contact resonance frequency of the cantilever (~300 kHz) and 1 *V* amplitude. Scansens cantilever tips with W_2C coating were used (curvature radius ~35 nm) for the measurements.

PL measurements were carried out using continuous wave He–Cd laser (wavelength 325 nm) with excitation power density typically less

than 0.6 W cm^{-2}. PL was measured at temperatures between 15 and 300 K using a closed cycle helium cryostat (APD *Cryogenic* closed-cycle helium system having two-stage cryogenic refrigerator DE-204SL with water-cooled helium compressor, based on the Gifford–McMahon cycle*)*. The luminescence was dispersed by a Spex 1704 monochromator (1 m, 1200 mm^{-1}) and detected by a cooled Hamamatsu R928 photomultiplier.

3. Results and discussions

3.1. Grain morphology and compositional determination

The morphological feature of the surface of sg-BCZT is shown in the FESEM image (magnification × 2k) in Fig. 1a. The microstructure revealed a morphology consisting of uniform distribution of grains separated by well-defined grain boundaries along with isolated intergranular pores. Grain size distribution with Gaussian fitting is shown in Fig. 1b. An estimated average size ~2.4 ± 0.42 μm was obtained. The apparent bulk density value was ~5.21 g/cm^3, which is ~90% of the theoretical density (5.78 g/cm^3).

To verify the compositional homogeneity in the sol-gel derived BCZT sample, elemental distribution was characterized using EDX technique. Compositional analysis was done using EDS spectrum (Fig. 1c) data and is summarized in Table 1. As seen, the obtained weight/atomic percentage of elements is in a good approximation to the expected values. Fig. 1d–h depict the elemental mapping images of the constituent elements (Ba, Ca, Ti, Zr and O) that are observed to be evenly distributed within the ceramic bulk.

To further substantiate the composition and chemical nature of the prepared sg-BCZT, x-ray photoelectron spectroscopy (XPS) was utilized, which is a well-established technique that provides information not only about the elemental composition but also about the chemical environment of the detected elements. The overview XPS scan spectrum of the fractured surface of the studied sample is shown in Fig. 2a, and one can perceive the relevant peaks of all the constituent elements *viz*. Ba, Ca, Zr, Ti, and O, along with the C 1*s* line of the residual carbon (at 284.77 eV). No other contaminant apart from carbon was detected on the sample surface. High-resolution spectra of the photoelectron peaks for each element were also measured and fitted. The core-level peaks of Ba 3*d*, Ti 2*p*, and O 1*s*, respectively are shown in Fig. 2(b–d). The patterns obtained are quite similar to those reported elsewhere [16]. The Ba 3*d* (Fig. 2b) core level peak exhibits two components: Ba $3d_{5/2}$ (at 779.06 eV; FWHM ~ 2.6 eV) and Ba $3d_{3/2}$ (at 794.38 eV; FWHM ~2.5 eV), that correspond to barium in $BaTiO_3$ [17]. For Ba 3*d* electron, the energy separation between the two peaks is about 15 eV, which is approximately the binding energy difference of Ba^{2+} ion to capture an electron [18]. Additionally, Ba 4*d* and Ba 4*p* peaks at 88.08 eV and 177 eV, respectively were also observed in the overview spectra (Fig. 2a), which are attributed to the different barium orbitals [17]. The peaks of Ti 2*p* located at 457.74 eV and 463.57 eV as seen in Fig. 2c correspond to the core levels of $Ti^{4+}2p_{3/2}$ and $Ti^{4+}2p_{1/2}$, respectively. Two sub-peaks located at 456.66 eV and 463.66 eV were identified post curve fitting, which can be attributed to $Ti^{3+}2p_{3/2}$ and $Ti^{3+}2p_{1/2}$ peaks, indicating the existence of Ti^{3+} species in the prepared BCZT [19]. The percentage composition of Ti^{4+} and Ti^{3+} was evaluated from the area of the fitted components and was found to be 94% and 6%, respectively. The presence of Ti^{3+} may be explained by the charge compensation for the oxygen vacancies. The formation of oxygen vacancies is accompanied by a change in the oxidation state of the nearest-neighbour Ti atoms from Ti^{4+} to Ti^{3+} in order to retain the local charge balance. The XPS spectra of O 1*s* in Fig. 2d exhibits two peaks centered at around 529.07 eV and 531.07 eV, which can be assigned to the lattice O^{2-} ions existing as Ba–O–Ti and Ti–O–Ti, respectively [20,21]. The core-level peaks from Zr 3*d* and Ca 2*p* are shown in Fig. 2e and f, respectively. The Zr 3*d* spectrum (Fig. 2e) comprises a doublet Zr $3d_{5/2}$–Zr $3d_{3/2}$, with spin-orbit splitting 2.41 eV. The Zr $3d_{5/2}$ having binding energy 181.05 eV corresponds to zirconium in the Zr^{4+} state [22]. The core-level peak of Ca 2*p* reveals the presence of a doublet (Ca $2p_{1/2}$ and Ca $2p_{3/2}$), with a difference in the binding energy of 3.52 eV indicating the presence of Ca^{2+} [23,24]. The atomic percentage (at%) of elements Ba (3d), Ca (2p), Zr (3d), Ti (2p), and O (1s), as calculated from the area under the respective element's peaks were: 14, 9, 5, 11 and 61, respectively.

Table 1
Elemental analysis results for sg-BCZT.

Element	Th. wt%	Exp. wt%	Th. at%	Exp. at%
Ba	52.36	52.58 ± 0.4	16.96	17.67
Ca	2.70	3.75 ± 0.39	3.13	4.19
Zr	4.09	4.41 ± 0.52	1.79	2.33
Ti	19.32	19.68 ± 0.4	17.86	19.07
O	21.53	19.58 ± 2.85	60.27	56.74

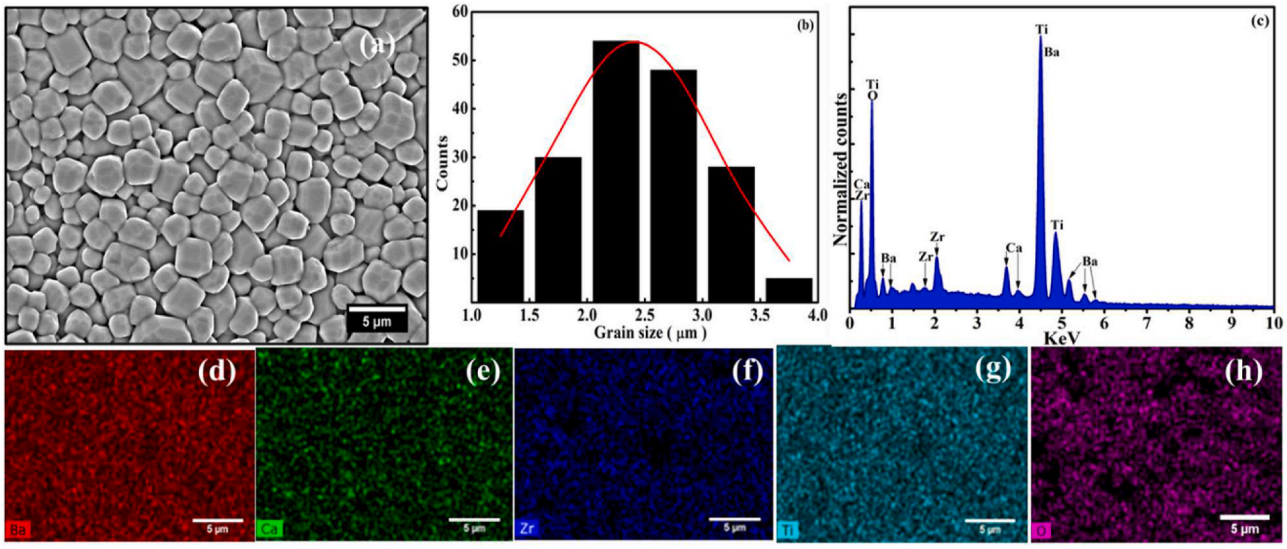

Fig. 1. **(a)** SEM micrograph of the as-sintered surface **(b)** grain size distribution **(c)** EDX spectrum. **(d-h)** elemental mapping distribution for individual elements (Ba, Ca, Zr, Ti and O).

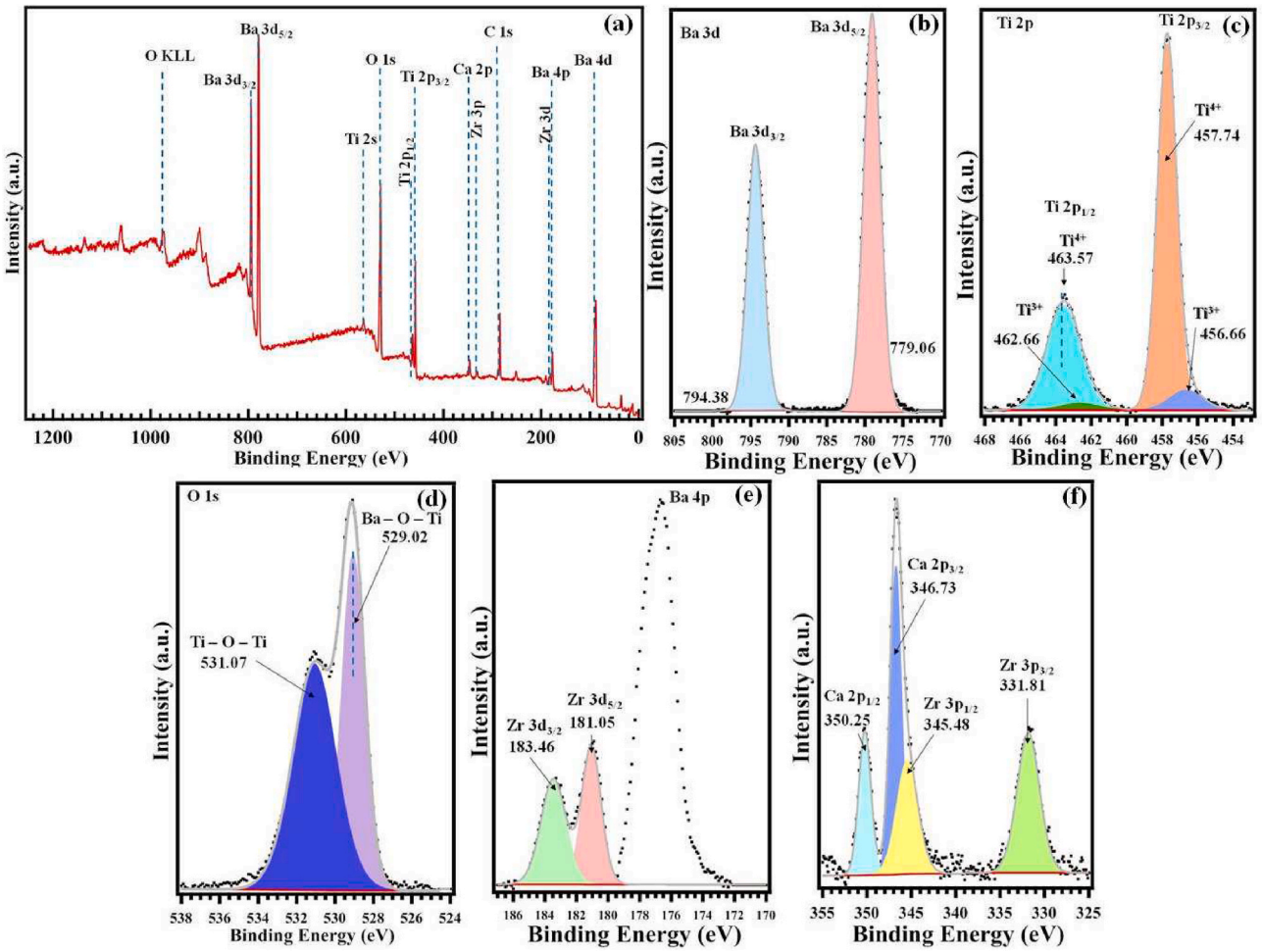

Fig. 2. **(a)** Overview XPS spectra. Core levels **(b)** Ba 3*d*, **(c)** Ti 2*p*, **(d)** O 1*s*, **(e)** Zr 3*d*, and **(f)** Zr 3*p*, Ca 2*p* in sol-gel derived BCZT ceramic. The black dots are experimental data while grey line represents envelope fitting.

3.2. X-ray diffraction

Fig. 3 demonstrates the room temperature XRD scan profile for the powdered sample of sintered sg-BCZT ceramics. No extra peaks/secondary phases were detected and there is a good agreement between the observed and calculated inter-planar spacing. This confirms the formation of a single-phase high purity BCZT compound.

Rietveld refinement on the full profile fitting of the XRD pattern was performed using the standard GSAS refinement software [25] with graphical interface EXPGUI [26]. Le Bail profile fitting was done before the crystal structural refinement. Scale-factors, zero-point, unit cell lattice parameters, isotropic displacement parameters (U_{iso}) and atomic positions were refined. Background correction was performed using shifted Chebyshev polynomial of the first kind. The diffraction peak profiles were fitted by pseudo-Voigt with Finger-Cox-Jephcoat peak asymmetry function which involves the refinement of the profile coefficients: Gaussian- 'GW', 'GV' (peak width parameters) and Lorentzian- 'LX' (crystallite size broadening), 'LY' (microstrain) and 'shft' (sample displacement). Refinement analysis revealed a co-existence of tetragonal, *T* (space group *P*4*mm*) and orthorhombic, *O* (space group *Amm*2) symmetries. The detailed list of Rietveld agreement factors and the crystal structure parameters of sg-BCZT are presented in Tables 2–4. The refined lattice parameters for the tetragonal phase in sg-BCZT (Table 2), when compared with the lattice parameters of pristine $BaTiO_3$, BTO (JCPDS:05–0626; space group: *P*4*mm*) shows shrinkage in the unit cell of sg-BCZT (0.012%, 0.62% and 0.65% in lattice parameters: *a*, *c* and volume, respectively). This can be interpreted in terms of the smaller ionic radii of the substituents Ca^{2+} (1.35 Å) and Zr^{4+} (0.72 Å) ions in comparison to their respective parent sites of Ba^{2+} (1.60 Å) and Ti^{4+} (0.86 Å) ions. To evaluate the structural parameters of pristine BTO, the corresponding crystallographic information file (for JCPDS:05–0626; space group: *P*4*mm*), was analysed using VESTA. The results are as follows: *B*–O(1): 2.1619 Å; *B*–O(1): 1.8707 Å; *B*–O(2): 2.0028 Å; *B* – *O*: 2.0073 Å; *D*: 0.0257; *QE*: 1.0040; polyhedral volume: 10.7484 $Å^3$. Here, *QE* represents the quantitative measure of polyhedral distortion, whereas the Baur distortion index, *D* simply considers the metal-ligand and the average bond length distances [27]. In comparison with BTO, a decrease in average bond length and polyhedral volume is observed in sg-BCZT (Table 4). Moreover, the difference between the two apical *B*–O(1) distances is higher in sg-BCZT (0.3695 Å) than that of BTO (0.2912 Å), implying a larger octahedral distortion of the BO_6 cage in sg-BCZT, which is implied by its higher *D* and *QE* [27]. All these parameters indicate a definite structural change on substitution with Ca^{2+} and Zr^{4+} ions in BTO. Lattice parameters and atomic positions obtained from Rietveld refinement were used to model the crystal structure. 3D rendering of the GSAS structural data obtained for the tetragonal phase was performed using the VESTA software package [28], and the same is shown as an inset of Fig. 3a.

Fig. 3b shows the XRD profile of Bragg reflection {200}, between −70 °C and 60 °C. Evident changes can be perceived in the profile shapes and positions with temperature. The rhombohedral (*R*3*m*) phase, which is typified by a singlet {200} with Miller index $(200)_R$ [29], can be seen at −70 °C. The orthorhombic distortion splits the {200} reflection into two peaks with Miller indices $(022)_O$ and $(200)_O$, evident at −50 °C.

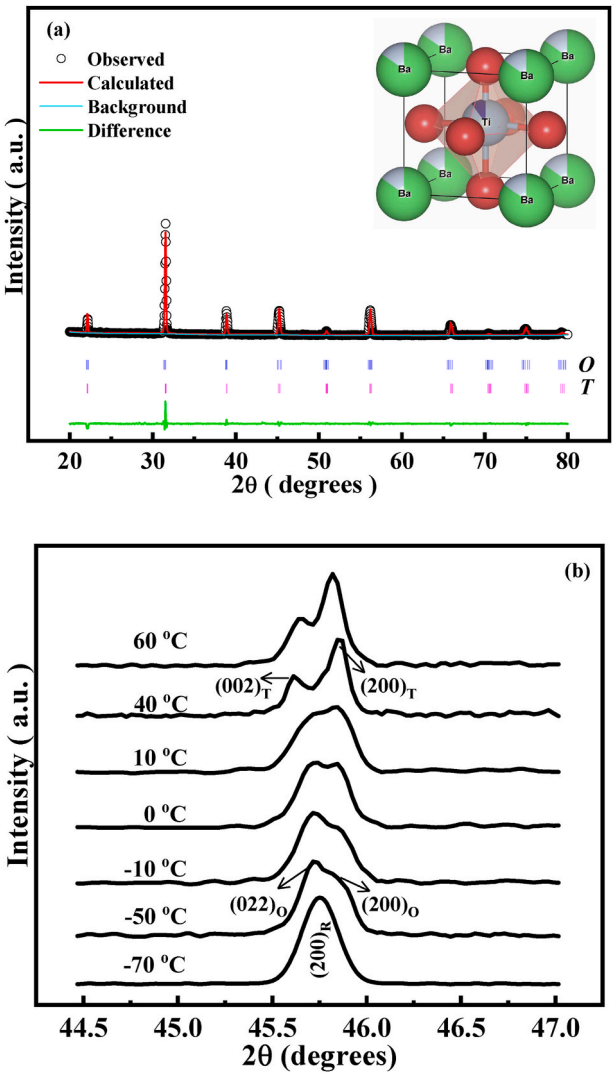

Fig. 3. (a) Rietveld graphical output of sg-BCZT ceramic. The small vertical bars indicate the position of reflections (T: tetragonal and O: orthorhombic phase). Inset shows the 3D interpretation of the crystal structure related to the tetragonal phase **(b)** Evolution of the {200} profile reflection peak with temperature. Miller indices of the peaks are marked.

Table 2
Rietveld agreement factors, unit cell parameters, unit cell volume and phase composition of sg-BCZT[a] sample. Values in parentheses represent the standard deviations.

No. of variables	28	
χ^2, R_F^2, R_{wp}	3.896, 8.57%, 10.25%	
Crystallographic system	Tetragonal	Orthorhombic
Space group	*P4mm*	*Amm*2
Weight fraction (%)	89.425(2)	10.575(1)
a (Å)	3.9985 (1)	3.9874(1)
b (Å)	3.9985 (1)	5.6751(1)
c (Å)	4.0076 (4)	5.6901(1)
Unit cell volume (Å^3)	64.073	
Tetragonality (*c*/*a*)	1.0023	

[a] There were 2282 observations for the refinement and the number of reflections was 114.

Table 3
Atomic coordinates and isotropic displacement parameters (U_{iso}) for sg-BCZT.

Atom	Wyckoff position	x	y	z	U_{iso}[a] (Å^2)
Crystallographic system: Tetragonal					
Ba	1a	0	0	0	2.2(4)
Ti	1b	1/2	1/2	0.520(3)	1.6(8)
O1	1b	1/2	1/2	−0.026(8)	0.75(2)
O2	2c	1/2	0	0.488(5)	0.79(3)
Crystallographic system: Orthorhombic					
Ba	2a	0	0	0	0.69(11)
Ti	2b	1/2	0	0.517(6)	0.56(17)
O1	2a	0	0	0.495(3)	0.46(4)
O2	4e	1/2	0.256(5)	0.246(7)	0.42(3)

[a] Given as 100 × U_{iso}.

Table 4
Structural parameters as obtained for the BO_6 octahedral sites in tetragonal phase of sg-BCZT. *A*-O and *B*–O represent bond lengths with *A*=(Ba,Ca) and *B*=(Ti, Zr).

Vector	Bond length (Å)
A-O(1) × 4	2.8326(12)
A-O(2) × 4	2.9157 (11)
A-O(2) × 4	2.7480(10)
B–O(1)	2.1885(14)
B–O(1)	1.8190(12)
B–O(2) × 4	2.0035(9)
Average bond length $\langle B-O \rangle$, (Å)	2.0036
Distortion index, *D*	0.0307
Quadratic elongation, *QE*	1.0057
Bond angle variance, BAV (deg^2)	10.188
Polyhedral volume (Å^3)	10.6789

On further increasing the temperature, the peaks gradually evolve into $(002)_T$ and $(200)_T$ peaks, marking a transition to the tetragonal phase at 40 °C.

3.3. Dielectric studies

Fig. 4a represents permittivity (ε_r) and loss tangent (tanδ) response obtained at 100 kHz. As can be realised, most of the anomalies are not very prominent and they appear as a broad hump. Diffuseness in transitions is attributed to the small grain size in the studied sg-BCZT sample [30]. Three inflections are perceptible in loss tangent behavior (denoted by *a*', *b*', c'), while two anomalies are observed in the ε_r plot (denoted by *a* and *b*). The *ferro-para*electric transition (tetragonal→cubic) is noticeable at ~105 °C (marked by "*a*" in Fig. 4a). However, the other inflection above room temperature (at "*b*") is barely discernible, highly diffused, and is a broadened feature. In conjunction with our XRD findings, this transition near 50 °C is the *ferro-ferro*electric phase transition (orthorhombic→tetragonal phase transition ($T_{O\text{-}T}$)). On moving further down the temperature, a broadened maximum in tangent loss curve is observed around −100 °C (marked as *c*'), which does not leave any imprint on the dielectric constant variation whatsoever. Analysis of this region, as depicted in the inset of Fig. 4c (right-hand corner) revealed that the tanδ maximum is frequency dependent, with its peak shifting towards higher temperatures with increasing frequency. These observations indicated that the associated phenomenon is a thermally activated process. An attempt, therefore, was made to verify the relaxation behavior using both, (a) the Arrhenius-type empirical relation [31],

$$f = f_o exp\left(\frac{-E_a}{k_B T}\right) \quad (1)$$

and (b) the complex '*freezing*' process described by the Vogel-Fulcher (VF) model [31]:

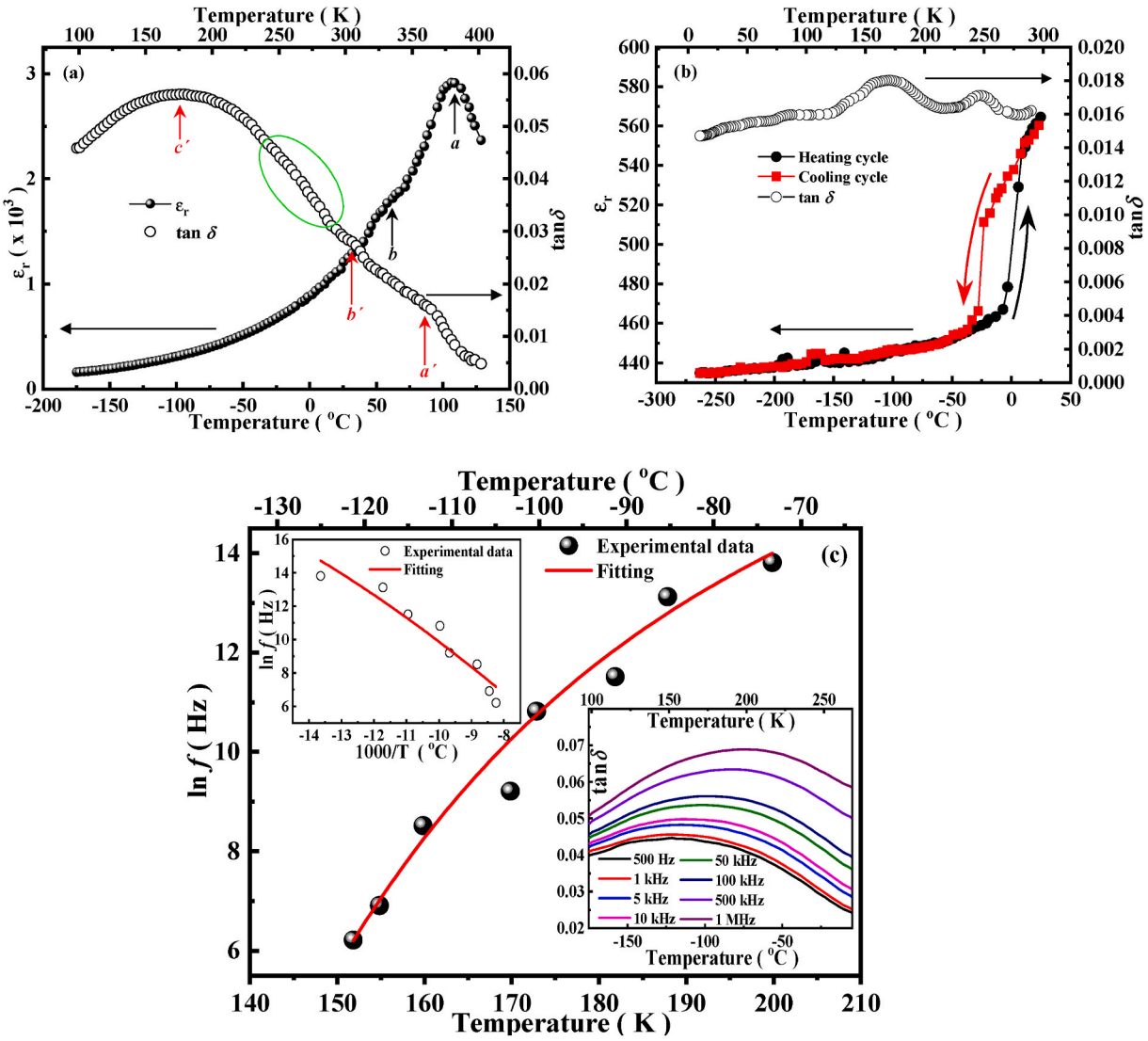

Fig. 4. Temperature dependence of permittivity and tangent loss at 100 kHz in the temperature range **(a)** −175 °C to 130 °C **(b)** −263 °C to 26 °C. **(c)** Vogel-Fulcher fit to the tanδ-maxima temperature in sg-BCZT. Insets in (c): inset on the top left corner represents Arrhenius fit while the inset at bottom right depicts the temperature dependence of tanδ collected at various frequencies.

$$f = f_o exp\left(\frac{-E_a}{k_B(T - T_{VF})}\right) \quad (2)$$

where f is the frequency of the applied field; f_o is the fundamental dipole frequency for polarization perturbation; E_a is the activation energy of the associated relaxation process; k_B is the Boltzmann constant and T is the temperature of tangent loss maxima, while T_{VF} is the Vogel-Fulcher temperature which represents the "*freezing*" temperature of the process. Inset of Fig. 4c (left-hand corner) represents fitting of the experimental data using Eq (1), which however resulted in an unrealistic value of $f_o = 1.57 \times 10^{19}$. A better fit was achieved using the Vogel-Fulcher model (Fig. 4c) that yielded fitting parameters: $f_o = 7.48 \times 10^9 \pm 3$ Hz, $E_a = 3.2 \pm 1.01$ meV and $T_{VF} = 123.25 \pm 6.77$ K. This relaxation phenomenon at low temperature in sg-BCZT samples is attributed to a local relaxation process in the R phase that also corresponds to the thermal-activated relaxation processes observed in mechanical and dielectric loss behavior in the rhombohedral phase of cobalt-doped BTO fine-grained ceramics [32].

At this juncture, it is worthwhile to discuss about the encircled temperature region (~−50 to 2 °C or 220–275 K) in Fig. 4a. To the naked eye, in a glimpse, nothing interesting can be noticed. However, one can perceive a subtle modulation in the loss curve, which may be crucial for further analysis, as it may provide an insight into the existence of subdued phase transitions at lower temperature that is also observed in parent BTO. Therefore, another dielectric measurement was performed using a different set-up consisting of Solartron 1260A impedance analyser equipped with a closed cycle autonomic cryostat (having two-stage cryogenic refrigerator DE-204SL with water-cooled helium compressor, based on the Gifford–McMahon cycle). It is specially designed for temperature range 10–300 K only and is sensitive to subtle changes in the sample behavior (but capable of measuring at a single frequency value at a time). The results obtained from this set-up is shown in Fig. 4b. It is clearly observed that there is indeed a presence of a transition in this temperature regime which is realised through the variation in both tangent loss and permittivity. Moreover, the discontinuity in permittivity variation undoubtedly proves the existence of a phase transition in this temperature range. The transition is of first-order as confirmed from the appearance of thermal hysteresis as also observed in BTO [33]. This phase transition corresponds to the rhombohedral → orthorhombic transformation ($T_{R\text{-}O}$). In Fig. 4b, one can also notice that the loss tangent maximum in the lower temperature region near −100 °C does not have any impression on the dielectric component, in accordance with what was seen in Fig. 4a.

3.4. Raman scattering investigation

3.4.1. Room temperature

Raman scattering is a highly sensitive spectroscopic technique to probe the local changes in the crystalline structure and can therefore serve as an effective tool to identifythe phase transitions. The absence of discrete dielectric anomalies made it difficult to clearly determine the phase transitions in the compound. Therefore, to validate the results of dielectric measurements and to explore the existence of additional phase transitions, if any, the Raman spectra were collected in the temperature range 8–680 K (−265 °C to 410 °C) for the sg-BCZT ceramic sample.

Fig. 5a displays the Raman spectra collected at room temperature in the range 10 cm^{-1} -1000 cm^{-1}. Peak positions of the phonon modes were estimated by Gaussian fitting. It is well-known that the Raman active phonon modes in a ferroelectric BTO with tetragonal crystal symmetry (C^1_{4v} point group), are represented by $3[A_1(TO) + A_1(LO)] + B_1 + 4[E(TO) + E(LO)]$ modes [34]. As compared to single crystals, the Raman lines appear broader in polycrystalline ceramics and the phonons lack true A_1, B_1 or E symmetry, because the phonon wavevectors are randomly oriented with respect to the crystallographic axes [35]. Interpretation of Raman spectra gets further complicated in the presence of compositional disorder occurring in A/B-site substituted compositions. For instance, in the present case, the substitution of Ti^{4+} by Zr^{4+} ions (having different ionic radius and mass) lead to the coexistence of two local octahedral environments in the perovskite structure of sg-BCZT. Moreover, the presence of non-polar [ZrO_6] clusters reduce the dipolar interactions between the polar [TiO_6] clusters in the lattice [36]. Such local structural distortions, effectively, may have other

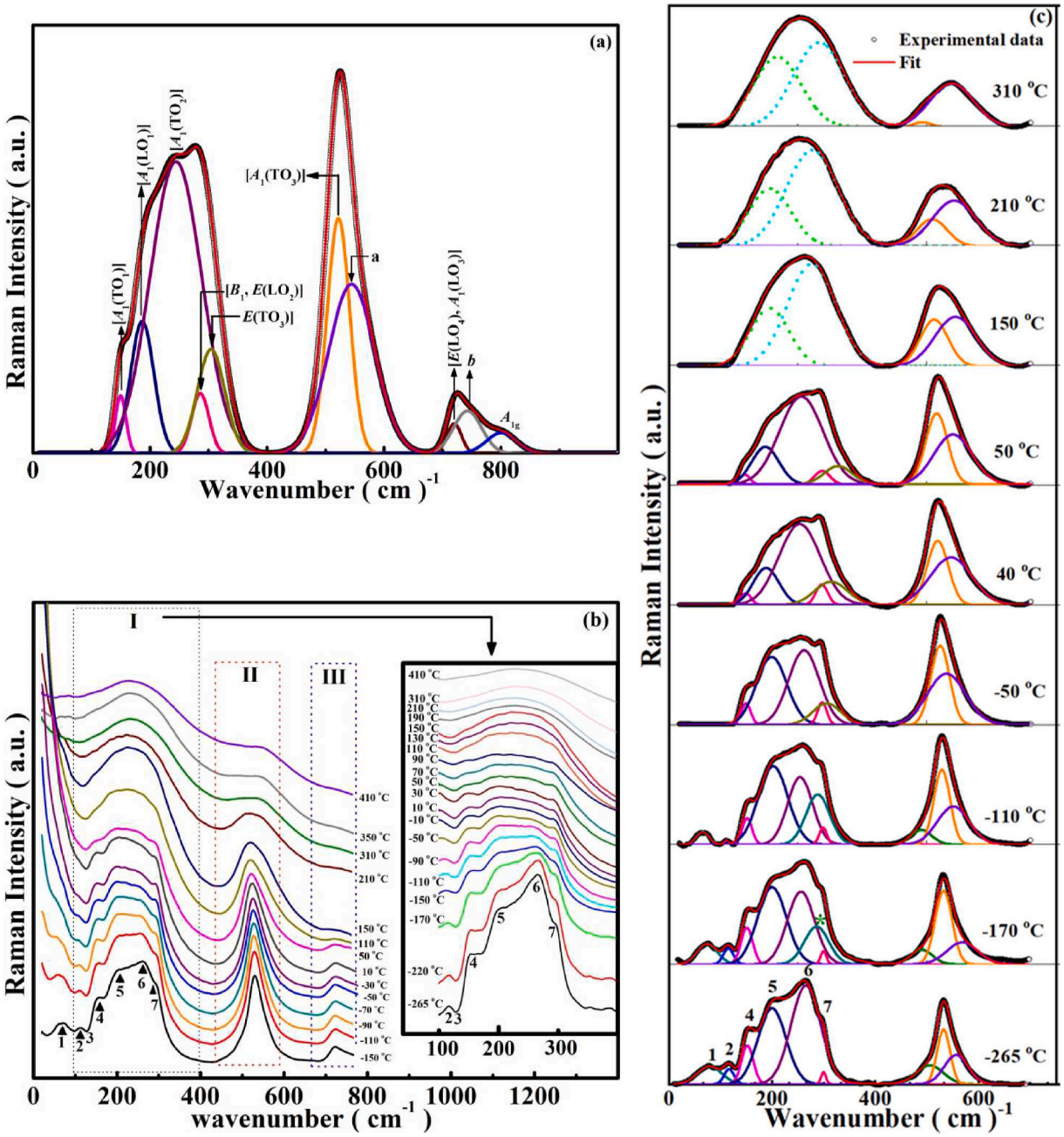

Fig. 5. **(a)** Room-temperature Raman spectrum of sg-BCZT collected in the range 10 cm^{-1} -1000 cm^{-1}. **(b)** Raman spectra at selected temperatures between −265 °C and 410 °C. Inset shows the amplified region of Raman spectra for wavenumber region 100-400 cm^{-1} and comprises spectra obtained at other in-between temperatures. **(c)** De-convoluted Raman spectra revealing the various modes.

consequences like additional spectral broadening, interference effects, shift in the Raman peak positions and appearance of extra Raman modes [**35**]. In our case, additional modes were observed: (i) ~800 cm^{-1} (A_{1g}), (ii) a major peak near 550 cm^{-1} (marked as 'a') and (iii) ~750 cm^{-1} (marked as 'b'). Observation of phonon mode near 550 cm^{-1} in BTO-based compositions has been reported by other authors as well. Its appearance is attributed to the breaking of Raman selection rules on account of changes in inter-atomic forces due to chemical substitution and/or high pressure [33,36,37]. In the present case, the cause is disorder in the Ti atom's position. The emergence of the other additional phonon mode ~750 cm^{-1} (marked as 'b'), is effectively splitting of the LO mode ascribed to the substitution by heavier zirconium ion [38–40]. The broad mode at ~800 cm^{-1} (A_{1g}) is an octahedral breathing-like mode stemming from the presence of two/more species at the B-site and it may occur irrespective of the existence or non-existence of a ferroelectric phase [40].

Characteristic bands observed in the ferroelectric phase of BTO and allowed by spectroscopic Raman selection rules were also observed: ~260 cm^{-1} [($A_1(TO_2)$)]; ~300 cm^{-1} ("*silent*" mode; [B_1, E(TO + LO)]), ~520 cm^{-1} ([$A_1(TO_3)$]) and ~720 cm^{-1} ([$A_1(LO_3)$, $E(LO_4)$]) [38,41]. The spectral dip near 180 cm^{-1} is less pronounced in the sg-BCZT composition which is otherwise prominent in BTO. Occurrence of this spectral dip is due to the anti-resonance caused by the anharmonic coupling among three A_1(TO) phonons. Moreover, the sharp peak at ~300 cm^{-1}, referred to as the "*silent*" mode, and one of the distinctive Raman signatures which in particular confirms the existence of long-range ferroelectric order in the material appears as a weak broad shoulder band in sg-BCZT. Largely, it can be concluded that substitution of Ca and Zr in BTO caused a marginal shift in few phonon modes, the appearance of additional modes and reduction of tetragonality (understood based on the suppression of intensities of the vibration modes, especially in the wavenumber range 200–300 cm^{-1}). The latter observation is in accordance with XRD results, where a decrease in tetragonality of the sg-BCZT compound in comparison to BTO was assessed.

3.4.2. Temperature dependence

Phase transitions in the sg-BCZT sample were investigated by monitoring the anomalies in phonon modes of Raman scattering measurements with temperatures varying from −265 °C to 410 °C. Fig. 5b delineates the evolution of Raman spectra between 10 and 800 cm^{-1} in the temperature range −150 °C to 410 °C, while the inset shows the expanded spectra in the low wavenumber region 100-400 cm^{-1} (region I of Fig. 5b and includes spectra for additional temperatures). With increasing temperature, the Raman modes grow broader and gradually lose intensity that assists in determining the phase transitions. However, it must be taken into account that most characteristics of the modes from *R* phase comprise those from *O* and/or *T* phase. Therefore, it is difficult to exclude the presence of the later or both phases and/or ascertain their appearance with temperature.

As shown in Fig. 5b (and its inset) and 5c, the presence of rhombohedral symmetry in the sample for temperatures at least below −50 °C can be figured out by the (a) existence of the so-called "*triple mode*" *i.e.* co-existence of peaks 2 (~115 cm^{-1}), 4 (~155 cm^{-1}) and 5 (~195 cm^{-1}), (b) non-existence of the overdamped soft mode and (c) presence of the mode $E(TO_4)$ at ~495 cm^{-1} [35,36,39]. It may be noted that the presence of peak 2 is associated with Zr–O motion and indicates the presence of Zr-based nano-sized clusters with local rhombohedral-type symmetry. The appearance of the other spectral dip (feature 3 in Fig. 5b) is due to the effect of interference between A_1(TO) phonons and emerges when chemically dissimilar BO_6 octahedra units coexist in the lattice structure [35,40]. With increasing temperature, the appearance of another mode (marked with asterisk in Fig. 5c) was observed, hinting at a transition near −170 °C. As the temperature increases, the phonon modes 1 and 2 progressively loses intensity and completely disappear above −50 °C. Likewise, it is seen that the intensity of mode $E(TO_4)$ is also lost at −50 °C. Moreover, the mode at ~65 cm^{-1} materializes into overdamped $E(TO_1)$ mode while the $E(TO_3)$ mode comes into prominence at and above −50 °C. Based on the above observations, it is concluded that sg-BCZT exhibits *R*-phase in the range −265 °C to −50 °C, before making a transition into the orthorhombic phase near −50 °C. With further increase in the temperature, we observe a progressive augment in the intensity of feature 7 (the '*silent*' mode), which becomes prominent in the vicinity of room temperature before slowly losing intensity beyond 50 °C. Additionally, around this temperature region there is a noticeable reduction in the intensity of [$A_1(TO_1)$] and [$A_1(LO_1)$] modes. Also, the spectral dip at ~180 cm^{-1} progressively disappears. These sluggish changes in this temperature range signify the transition to tetragonal phase, however, with a strong possibility of a co-presence of the ferroelectric orthorhombic and tetragonal phases because of the similar Raman spectra characteristics for *O* and *T* phases [42]. As the temperature increases further beyond 110 °C, the onset of the cubic paraelectric phase is marked by a significant broadening of the band centered at about 270 cm^{-1} (region I), asymmetric bands in the vicinity of 520 cm^{-1} (region II) and 725 cm^{-1} (region III). This is also accompanied by merging and complete loss of the intensity gap between 3 and 5 above 110 °C, along with the disappearance of [$A_1(TO_1)$] mode. These variations undeniably indicate the *ferro-para*electric *T*→*C* transition (T_c). Although broadened, however, the bands in the regions I and II persist well beyond T_c. Normally impermissible in the centrosymmetric cubic phase, the persistence of these phonons beyond T_c is ascribed to the presence of non-centrosymmetric regions originating from strong lattice disorder of Ti ion position along the cube diagonals [43,44] or may be related to the presence of disorder-induced first-order Raman scattering [45]. Hitherto, the analysis of Raman spectra with temperature indicated the following transition sequence in sg-BCZT: $R \xrightarrow{-50\pm10\ ^{\circ}C} O \xrightarrow{40\pm10\ ^{\circ}C} T \xrightarrow{110\ ^{\circ}C} C$; though without any conclusive/clear signature of the *ferro-ferro*electric structural transformation *O*→*T* and the subtle transition near −170 °C.

Therefore, in order to validate the transitions with more clarity and realize the subtle changes that may have occurred for the transitions, Raman scattering measurements were performed at a very small temperature interval of 0.4 °C. To verify the temperature-driven structural changes, analysis of the results has been done in terms of variations in the band characteristics, *viz.* linewidth, intensity, and frequency shift of the optical phonons lines.

Fig. 6 illustrates the results obtained for the optical Raman modes at: ~520 cm^{-1}[$A_1(TO_3)$]; ~495 cm^{-1} [$E(TO_4)$] and ~550 cm^{-1}. The various phase transitions are manifested through discontinuities and slope changes in the temperature versus line width, wavenumber, and intensity curves. Fig. 6a displays the evolution of the intensity for the [$E(TO_4)$] and [$A_1(TO_3)$] modes with temperature. The anomalies indicating phase transitions are identified in the plot. The intensity of vibration mode [$E(TO_4)$] continuously weakens with rising temperature and progressively drops to zero at around −50 °C, marking the *R*→*O* transition. A slope change was perceptible at ~45 °C, indicating the *O*→*T* phase transition. It is also noticed that the *T*→*C* transition at the Curie temperature is partial and that there is a simultaneous existence of residual ferroelectric symmetry into the cubic phase. The reason behind this phenomenon is well-documented and has been discussed in the previous section. Inset in Fig. 6a shows the variation of the intensity of vibrational line at ~520 cm^{-1} ([$A_1(TO_3)$]) over the complete temperature span −265 °C to 410 °C. This particular mode is known to be proportional to the dielectric anomaly through the fluctuation-dissipation theorem [46,47]. The detectable slope changes substantiate the different transitions and agree with those observed in the tangent loss curve (Fig. 4a and b). The minor inconsistency between the phase transition temperature values obtained by the two methods is due to the much smaller coherence length and time scale of the physical event measured by Raman investigation as compared to dielectric measurements. Apart from the confirmed transitions, it was interesting to note an additional slope change in the [$A_1(TO_3)$] mode (along with that in the

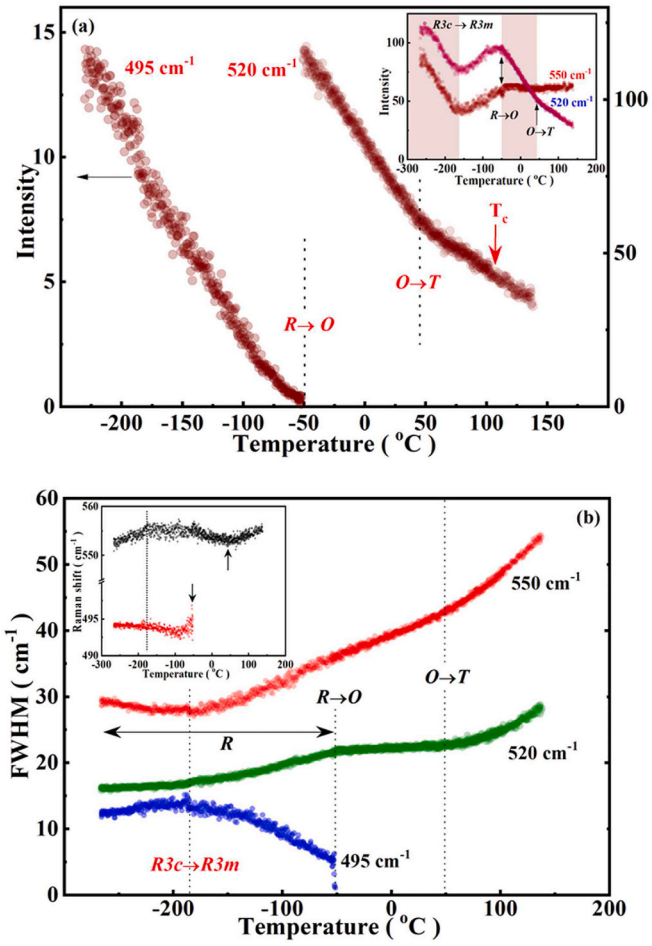

Fig. 6. **(a)** Temperature dependence of the intensity of vibrational lines ~495 cm^{-1}, [$A_1(TO_3)$] and ~520 cm^{-1}, [$E(TO_4)$] phonon modes. The various transitions are marked. Inset shows the variation of intensity for vibration lines ~520 cm^{-1} and ~550 cm^{-1} for the temperature range −265 °C–140 °C. The different phase transitions are evidenced. **(b)** Temperature dependence of bandwidth for vibration lines ~495 cm^{-1}, ~520 cm^{-1} and ~550 cm^{-1}. The regions are demarcated by dashed lines. Inset shows the variation of peak shift in vibration lines ~495 cm^{-1} and ~550 cm^{-1} with temperature.

vibrational line ~550 cm^{-1}), indicating a transition near −175 °C which has never been reported in the parent BTO compound. Very likely, as also observed in PZT, it is an indication of a transformation from low-temperature rhombohedral *R*3c phase to high-temperature rhombohedral phase with symmetry *R*3m. This transition *R*3c→*R*3m was signalled by the appearance of the mode near 285 cm^{-1} and also reflected by the gradual broadening of peak 6 near −170 °C (inset of Fig. 5b), which was otherwise sharp below −170 °C. From the perspective of symmetry, the *R*3m→*R*3c transition is usually associated with an instability of the Brillouin zone corner producing an altered oxygen octahedral tilt [48,49]. This transitional event did not appear in the dielectric measurements; an observable fact often experienced in ferroelectrics in which phase transformations have an effect on Raman modes or elastic properties but are not reflected in their dielectric behavior [50].

The temperature variation of the bandwidth (FWHM) of [$A_1(TO_3)$], [$E(TO_4)$] and mode ~550 cm^{-1} demonstrated distinct slope changes and loss of bandwidth, as seen in Fig. 6b. The modes at ~550 and 520 cm^{-1} show broadening as the temperature increases, while the $E(TO_4)$ mode weakens with increasing temperature and is finally lost near −50 °C. Likewise, the variation in frequency shift of vibration lines ~495 cm^{-1} and ~550 cm^{-1} with temperature (inset Fig. 6b), point out phase transitions near −50 °C and ~45 °C. Apart from these transitions, additional slope change in all the curves is noted that indicates a transition near −180 °C, which has been discussed above.

To summarize, the exhaustive analysis of Raman and dielectric results accommodate the following phase transition sequence: $R\,(R3c) \xrightarrow{-175\pm10\,^{\circ}C} R\,(R3m) \xrightarrow{-50\pm10\,^{\circ}C} O - \;T \xrightarrow{40\pm10\,^{\circ}C} T \xrightarrow{120\pm10\,^{\circ}C} C$. All these observed changes correlate with the modifications in the short-range order that evolves upon reorganization of the respective *R*, *O*, *T* and *C* phase fractions.

3.5. Temperature dependence of photoluminescence emission

It is well known that typical ferroelectric insulators become semiconductors upon doping, which form donor or acceptor levels below the conduction band or above the valence band, respectively [51]. The band structure of ferroelectric oxides is characterized by a band gap determined mainly by the potential within the unit cell, implying that any perturbation of the symmetry in the unit cell will affect the electronic structure and the energy band gap. Extensive theoretical investigations of the $BaTiO_3$ perovskite structure have shown that the energy band gap increases at every ferroelectric phase transitions upon cooling starting from the cubic structure to tetragonal to orthorhombic and rhombohedral [52,53]. These observations are also consistent with the Varshni relation for the temperature dependence of semiconductor band gap: $E_g(T) = E_g(0) - \alpha T^2/(T+\beta)$, where $E_g(T)$ is energy gap of the material at temperature *T* K, $E_g(0)$ is energy gap at 0 K, and α, β are constants. In this regard, PL spectroscopy which is a widely used technique for characterization of the optical and electronic properties of materials, can be used to extract valuable information about semiconductor materials and serve as a non-contact method to probe structural phase transition processes involving changes in energy band gap like in ferroelectric transitions. Evidently, this non-destructive and a highly sensitive PL spectroscopy method has been employed to investigate phase transitions in $BaTiO_3$-, PZT-, $SrTiO_3$-based oxide perovskites [54–58], halide perovskites [59,60], phosphors [61], etc.

Fig. 7 illustrates the temperature dependence of PL emission spectra of the sg-BCZT sample obtained over a temperature range of 15 K–300 K and under the excitation of a laser beam with a wavelength of 325 nm (~3.81 eV). The PL emission spectra exhibits a broad band covering a large part of the visible spectra. While above 220K, the emission spectra markedly change near the wavelength range ~600–620 nm, that can be perceived in the inset 1 of Fig. 7. The intensity of the PL bands is observed to significantly increase with decreasing temperature. Inset 2 shows the temperature dependence of the intensity of the PL band near 610 nm. It is important to recognise that since no photoluminescence radiative center (e.g. rare-earth) was intentionally added to sg-BCZT, the observed emission is therefore due to the existence of intrinsic defects rather than to an extrinsic PL mechanism. Also, since the excitation energy is lower than the band gap value in the rhombohedral phase (~4.9 eV) [52], the observed broad PL band is attributed to certain localized luminescence states/electronic states within the band gap. The electronic band structure of ordered parent compound BTO has conduction bands made of Ti−3*d* orbitals and valence bands made up of O−2*p* states separated by a band gap, while in BCZT, the conduction band will also be composed of Zr−4*d* orbitals, as seen in the representative wide band model, Fig. 8a. The localized states in the band gap are associated with self-trapped excitons (STEs), lattice distortion, defects or impurity levels [62]. The presence of localized states favours trapping of electrons (e') and holes ($h^{\bullet}$) during the excitation process. Theoretical and experimental results have shown that defect complex clusters like [$ZrO_5 \cdot V_O^z$] and/or [$TiO_5 \cdot V_O^z$], act as radiative centres [63,64]. Defects like oxygen vacancies ($V_O^z = V_O^x,\ V_O^{\bullet}$ *or* $V_O^{\bullet\bullet}$) play a vital role in creating STEs (composed of bound excitons). Electrons from the deep (or shallow) hole traps, on absorbing photons are excited to some localized sensitizing centres (deep or shallow electron traps), thereby creating

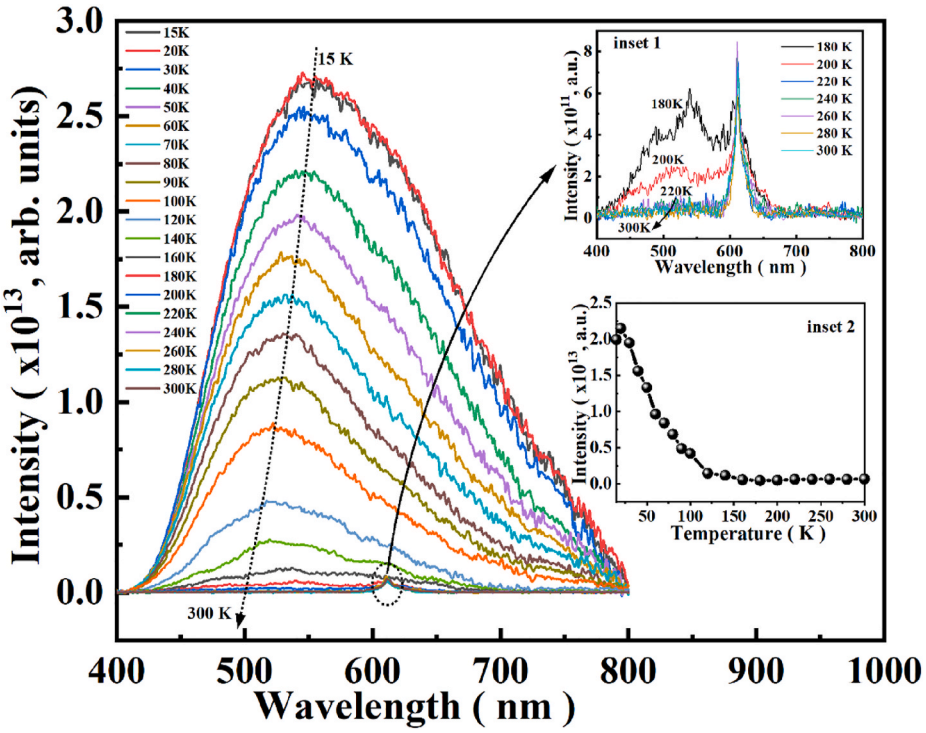

Fig. 7. Evolution of photoluminescence spectra in sg-BCZT with temperature from 15 K to 300 K. Inset 1 shows the magnified image of the PL emission spectra for the temperature range 180K–300K and inset 2 illustrates the temperature dependence of peak intensity of the emission band near 600 nm.

small polarons [65]. These electron polarons interact with holes, possibly trapped in defects or impurities, and form intermediate states called the self-trapped excitons that contribute to the visible PL emission [63]. Moreover, our XPS results pointed to the existence of Ti^{3+} in the sg-BCZT sample. The Ti^{3+} also acts as radiative centres and cause luminescence due to recombination of an electron trapped by Ti^{3+} with a hole [65,66]. In $SrTiO_3$, it has been established that the red luminescence band centered at around 2.0 eV is associated with trapped Ti^{3+} polarons in the close vicinity of the vacancy [66].

On the other hand, in the orthorhombic phase for which the experimentally determined band gap value is ~3.4 eV [52], the emission peak in the sg-BCZT sample is observed to be relatively sharper as compared to that in the *R*-phase. It was noted that in the temperature between 220 and 300 K, only the orange emission component with photon energy ~2.03 eV is dominant. This luminescence state is located within the energy band gap. Since with increasing temperature the population of bound excitons decreases, the recombination rate is also very low [67]. It is possible that in this temperature region, only the transition between deep defects is active. Moreover, this development of reduction in population of bound excitons and the ensuing low recombination rate, causes the PL intensity to reduce drastically (as observed in the inset 2 of Fig. 7).

In order to acquire quantitative description of the PL response of the sample, the emission spectra were deconvoluted by curve-fitting using the Gaussian function and a few representative fitted PL spectra are shown in Fig. 8b–e. It is realised that the luminescence band varies from blue to red spectral region with distinct bands or colour components showing their respective photon energy maxima at ~485 nm (~2.56eV: blue), 530 nm (~2.34eV: green), 612 nm (~2.03eV: orange) and between 650 and 750 nm (~1.91–1.65eV: red). The blue emission is associated with shallow defects in the band gap, whereas green-orange-red emission components are related with deep defects (like $[TiO_5 \cdot V_O^{\bullet\bullet}]$ complex clusters) [68,69].

To examine the variation in PL wavelength, the peak wavelength was plotted as a function of temperature, as depicted in Fig. 8f. It can be seen that while the position of the PL wavelength does show a variation with temperature, the trend is far from smooth and there are discontinuities in the wavelength shift. These discontinuities correspond to the BCZT crystal structure undergoing phase transition. The anomalies arise because the individual crystal structure have different bandgaps (attributed to the different orbital overlaps within the phases), resulting in the PL wavelength to deviate at the phase transition temperature. For example, let us consider the shift of peak wavelength associated with the orange emission component (near 612 nm). As the sample is cooled from 300 K, negligible shift is observed, however, near 220 K (~−53 °C), a discontinuity is observed indicating the transition from the *O*-phase into the *R*-phase. As the temperature is decreased further, a blue shift is observed indicating widening of the band gap. This is the general observation in ferroelectric perovskites and also consistent with Varshni relation, as discussed above. With further cooling, another anomaly is observed near 100 K (~−173 °C), pointing to another transition, believed to be associated with the change in symmetry of the unit cell from *R3m* to low-temperature *R3c* of the rhombohedral phase. Interestingly, below 100 K a red shift is observed, implying narrowing of the band gap which is opposite to the general trend observed with decreasing temperature. The transition *R3m* → *R3c* corresponds to an instability of the Brillouin zone corner point resulting from tilt of the oxygen octahedra. Possibly, the decreased orbital splitting and changes in the electron-phonon coupling causes the band gap to become narrower [70,71]. Also, on comparing Fig. 8c and d, it is noticed that a new band centered at near 560 nm (~2.2 eV) appears in the spectrum near 100 K, further supporting the transition *R3m* → *R3c*. Thus, the PL spectroscopy investigation suggests orthorhombic to rhombohedral (*R3m*) and *R3m* → *R3c* phase transition temperatures at 220 ± 10 K (−53 ± 10 °C) and 100 ± 10 K (−173 ± 10 °C), respectively that corroborate the findings from Raman and dielectric studies.

3.6. Piezoresponse force microscopy (PFM)

Temperature-induced modifications in the domain configuration associated with phase transitions were investigated using the PFM technique that was performed on the polished surface of sg-BCZT

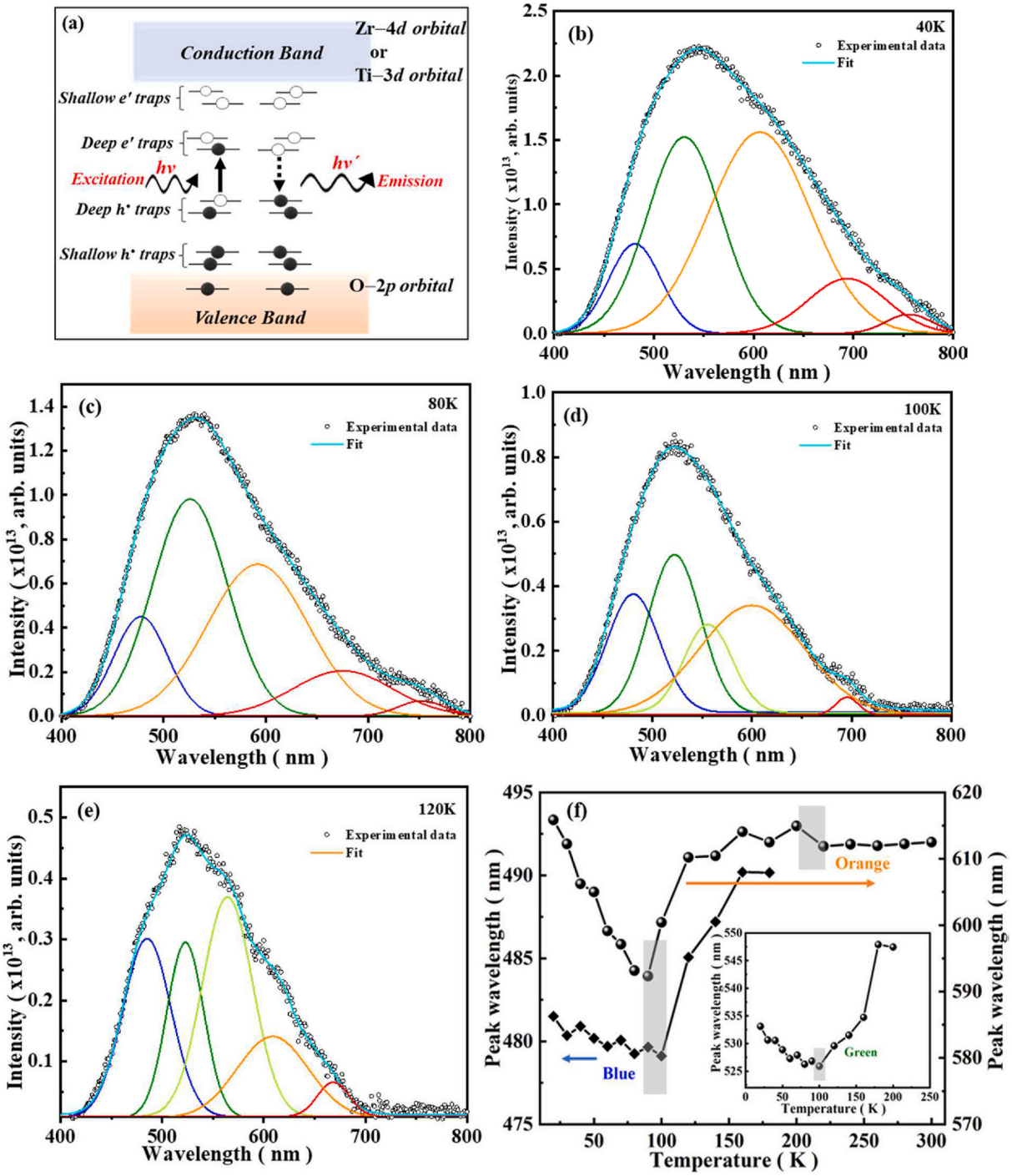

Fig. 8. (a) Wide band model showing the PL process. Excitation → formation of STE, and after excitation → recombination of e' and $h^{\bullet}$ for the PL emission (b–e) Deconvolution of PL spectra into individual emission peaks (colour components: Blue; Green; Orange and Red) at selected temperatures, and (f) Temperature dependence of PL peak position for wavelength ~600 nm (orange), ~480 nm (blue) and ~530 nm (green; shown in the inset). (For interpretation of the references to colour in this figure legend, the reader is referred to the Web version of this article.)

sample. Dual AC Resonance Tracking (DART) mode was employed for the measurements to gain resonance amplification. Vertical piezoresponse force microscopy (VPFM) was conducted on a scan area of size 3 × 3 μm^2. This representative region was investigated to record the development of domain pattern during the transition from a mixed orthorhombic-tetragonal to tetragonal and finally to the paraelectric cubic phase. During domain imaging, the temperature of the sample was initially increased from 25 °C to 120 °C at a rate of 5 °C/min, and subsequently cooled to 25 °C.

Fig. 9a shows the surface topography image that reveals a typical sintered polycrystalline structure with grains and defects (grain boundaries and pores). Fig. 9(b–g) illustrate the piezoresponse amplitude images acquired at different temperatures. As visible, the room-temperature amplitude image (Fig. 9b) shows a complex domain pattern with regions of positive, intermediate, and negative piezoresponse. The PFM image reveals a polarisable matrix embedded predominantly with nanoscale blotchy domains having unclear/fuzzy domain boundaries. It may be noted that the nanosized domains were

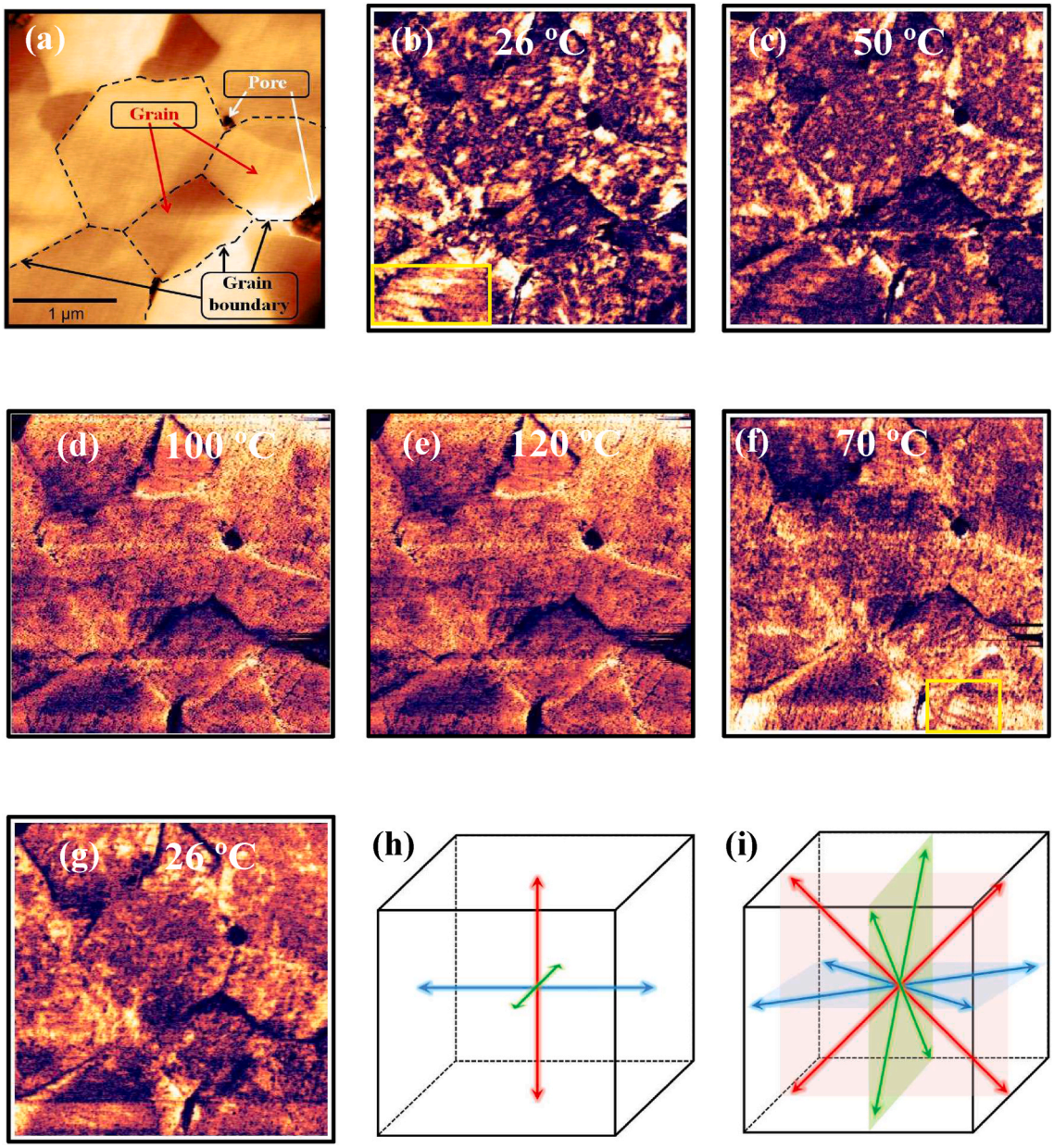

Fig. 9. (a) Surface topography showing grains, grain boundaries and pores. (b–f) Vertical PFM amplitude images at various temperatures. Images (b)–(e) represent heating cycle from 26 °C to 120 °C while (f),(g) show images through cooling. Schematic representation of the orientation of the polarization axes in $BaTiO_3$ in its (h) tetragonal, *T* and (i) orthorhombic, *O* phase. It shows the 6 possible and energetically equivalent directions of polarization vector along the edges of unit cell in *T* state, as compared to 12 possible directions available along the face diagonals in *O* state.

too small to be resolved by PFM. However, the grain in the lower left-hand corner (marked with a yellow box in Fig. 9b), reflected a domain pattern with deformed lamellar domains. The typical patterns of the ferroelectric domain (lamellas and herringbones) as usually observed in $BaTiO_3$ ceramics are lacking in the present case. It is possibly due to the formation of a complex combination of domain patterns owing to the coexistence of tetragonal and orthorhombic domains in the small grains. The tetragonal structure allows six polarization directions ⟨001⟩ (Fig. 9h) while the orthorhombic symmetry possesses 12 possible and energetically equivalent polarization directions ⟨110⟩ along the face diagonals (Fig. 9i). Observation of nanodomain structure has been reported in local piezoresponse studies of $(K,Na)NbO_3$-based polycrystalline ceramics [72]. In few papers on piezoelectrics with coexistence of two phases, miniaturization of domains to the nanometer scale assembled in lamellar-shaped domain frames have been reported [73,74]. It is known that materials with fine grains show typical small irregularly shaped patterns [72]. This is attributed to the fact that domain development is strongly dependent on microstructural characteristics (grain size, density) and crystalline structural modifications, and therefore affected by different synthesis methods, sintering parameters, or stress conditions [75,76]. Additional boundary conditions, inhomogeneous intragranular stresses or local inhomogeneous compositions, may also promote irregularities in domain morphology [77]. Taking the above arguments into consideration, it is quite evident that the predominance of nanodomains resulting from the complex interplay of intragranular stress compensation and/or structural, chemical disorder could be hindering the formation of a homogeneous domain contrast in PFM scans [78].

As the temperature was raised to 50 °C (Fig. 9c), a reorganization in the domain pattern is observed accompanied with a change of the direction of polarization. For instance, if we focus on the boxed corner of the image (Fig. 9b) and compare it with that of Fig. 9c, a change of

contrast is perceived. At this temperature, the sample is in the transition stage from orthorhombic to *T*-phase. On further increasing the temperature to 120 °C (Fig. 9e), the domains fade away, and the amplitude of piezoresponse significantly decreased. The dissolution of domains at higher temperatures implies transition into the paraelectric cubic phase. It may however be noted that a weak piezoresponse contrast is observed at 120 °C (*i.e.* even beyond T_c). Similar PFM observations have been reported on the ferroelectric phase transition studies in triglycine sulphate [79], $BaTiO_3$ (100) surfaces [80], (1-x)$PbMg_{1/3}Nb_{2/3}O_3$-*x*$PbTiO_3$ [81] and $Bi_{1/2}Na_{1/2}TiO_3$–$BaTiO_3$ single crystals [82]. In the present case, the seemingly weak piezoresponse contrast could probably be due to topographic crosstalk. Domains reappeared when the sample was cooled to room temperature. It may be noted that a region having wedge-shaped domains could be identified at 70 °C (yellow box in Fig. 9f) near the tetragonal phase transition.

4. Conclusions

$(Ba_{0.85}Ca_{0.15})(Zr_{0.10}Ti_{0.90})O_3$ ceramics were obtained by sol-gel chemical route (sg-BCZT). Rietveld refinement of the XRD data revealed a co-existence of tetragonal, *T* (space group *P4mm*) and orthorhombic, *O* (space group *Amm*2) symmetries. Phase transition temperatures were independently determined from the temperature dependence of XRD, anomalies in the ε_r -T plots, PL spectroscopy and was also validated with temperature-dependent Raman spectroscopy measurements. A transition *R3c* to *R3m* which is generally not observed in BTO compound, was revealed in BCZT. The variation of peak positions of PL spectra as a function of temperature corroborated the transitions *R3c→R3m and R→O phase*. Moreover, the quantitative analysis of the PL spectra indicated the existence of localized states in the band gap and intrinsic presence of trapped holes and electrons, which allow photoluminescent emission in the visible spectral region. Additionally, the local piezoresponse force microscopy experiments showed apparent changes in the domain configuration implying the occurrence of phase transitions. It is concluded from the corroborative XRD, dielectric, Raman and PFM results, that the BCZT ceramic sample obtained by sol-gel method exhibits the following phase sequence: $R\ (R3c) \xrightarrow{-175\pm10\ ^\circ C} R\ (R3m) \xrightarrow{-50\pm10\ ^\circ C} O \xrightarrow{40\pm10\ ^\circ C} T \xrightarrow{120\pm10\ ^\circ C} C$.

CRediT authorship contribution statement

Indrani Coondoo: Conceptualization, Validation, Methodology, Investigation, Formal analysis, Writing – original draft, Writing – review &; editing. **Alexander Krylov:** Investigation, Formal analysis. **Dhananjay K. Sharma:** Investigation, Formal analysis, Software, Writing – review &; editing. **Svetlana Krylova:** Investigation, Formal analysis. **Denis Alikin:** Investigation, Software. **J. Suresh Kumar:** Investigation, Writing – review &; editing. **A. Mirzorakhimov:** Investigation, Formal analysis. **Nina Melnikova:** Investigation, Formal analysis. **Manuel J. Soares:** Investigation, Writing – review &; editing. **Andrei L. Kholkin:** Writing – review &; editing, Supervision.

Declaration of competing interest

The authors declare that they have no known competing financial interests or personal relationships that could have appeared to influence the work reported in this paper.

Acknowledgements

I.C. and J.S.K would like to acknowledge financial assistance by national funds (OE), through FCT – Fundação para a Ciência e a Tecnologia, I.P., in the scope of the framework contract foreseen in the numbers 4, 5 and 6 of the article 23, of the Decree-Law 57/2016, of August 29, changed by Law 57/2017, of July 19. This work was developed within the scope of the project CICECO-Aveiro Institute of Materials, UIDB/50011/2020 & UIDP/50011/2020, financed by national funds through the FCT/MCTES. This work was partially developed within the scope of the project i3N, UIDB/50025/2020 & UIDP/50025/2020, financed by national funds through the FCT/MEC. Part of this work (A.K.) was supported by the Ministry of Science and Higher Education of the Russian Federation (grant no. 075-15-2021-588). This research used resources of the Ural Center for Shared Use "Modern nanotechnology", Ural federal University, Russia and the Krasnoyarsk Regional Center of Research Equipment of Federal Research Center "Krasnoyarsk Science Center SB RAS". The authors thank Dr. Gonzalo Irurueta, Center for Mechanical Engineering and Automation, University of Aveiro, Portugal and Dr. E. Venkata Ramana, Department of Physics, University of Aveiro, Portugal.

References

[1] K. Uchino, Ferroelectric Devices, Marcel Dekker, New York, 2000 ch. 7.
[2] B. Jaffe, Piezoelectric Ceramics, Academic Press, New York, 1971 ch. 7.
[3] Y. Saito, H. Takao, T. Tani, T. Nonoyama, K. Takatori, T. Homma, T. Nagaya, M. Nakamura, Lead- free piezoceramics, Nature 432 (2004) 84–87.
[4] T. Takenaka, K.-I. Maruyama, K. Sakata, *$(Bi_{1/2}Na_{1/2})TiO_3$—$BaTiO_3$ System for lead-free piezoelectric ceramics*, Jpn. J. Appl. Phys. Part 1 (30) (1991) 2236–2239.
[5] B.J. Chu, D.R. Chen, G.R. Li, Q.R. Yin, *Electrical properties of $Na_{1/2}Bi_{1/2}TiO_3$–$BaTiO_3$ ceramics*, J. Eur. Ceram. Soc. 22 (2002) 2115–2121.
[6] W.F. Liu, X.B. Ren, Large piezoelectric effect in Pb-free ceramics, Phys. Rev. Lett. 103 (2009) 257602.
[7] I. Coondoo, N. Panwar, D. Alikin, I. Bdikin, S.S. Islam, A. Turygin, V.Y. Shur, A. L. Kholkin, A comparative study of structural and electrical properties in lead-free BCZT ceramics: influence of the synthesis method, Acta Mater. 155 (2018) 331–342.
[8] K. Castkova, K. Maca, J. Cihlar, H. Hughes, A. Matousek, P. Tofel, Y. Bai, T. W. Button, *Chemical synthesis, Sintering and piezoelectric Properties of $Ba_{0.85}Ca_{0.15}$ $Zr_{0.1}Ti_{0.9}O_3$ lead-free ceramics*, J. Am. Ceram. Soc. 98 (2015) 2373–2380.
[9] X.W. Wang, B.H. Zhang, G. Feng, L.Y. Sun, Y.C. Shi, Y.C. Hu, J. Shang, S.Y. Shang, S.Q. Yin, X.E. Wang, *Effects of calcining Temperature on Structure and Dielectric and ferroelectric Properties of sol-gel synthesized $Ba_{0.85}Ca_{0.15}Zr_{0.1}Ti_{0.9}O_3$ ceramics*, J. Elec mater 49 (2020) 880–887. W. Kang, Z. Zheng, Y. Li and R. Zhao, The influence of sintering temperature on the microstructures and electrical performances of BCZT ceramics, Mater. Lett., 265 (2020) 127298.
[10] S. Belkhadir, S.B. Moumen, B. Asbani, M. Amjoud, D. Mezzane, I.A. Luk'yanchuk, E. Choukri, L. Hajji, Y. Gagou, M. El Marssi, *Impedance spectroscopy analysis of the diffuse phase transition in lead-free $(Ba_{0.85}Ca_{0.15})(Zr_{0.1}Ti_{0.9})O_3$ ceramic elaborated by sol-gel method*, Superlattice. Microst. 127 (2019) 71–79.
[11] P. Jaimeewong, P. Ngernchuklin, N. Promsawat, S. Pojprapai, S. Jiansirisomboon, M. Promsawat, A. Watcharapasorn, Characterization of phase evolution, microstructure and electrical properties of sol-gel auto-combustion derived BCZT ceramics, J. Nanosci. Nanotechnol. 18 (2018) 4230–4235.
[12] X. Ji, C. Wang, S. Zhang, R. Tu, Q. Shen, J. Shi, L. Zhang, Structural and electrical properties of BCZT ceramics synthesized by sol-gel-hydrothermal process at low temperature, J. Mater. Sci. Mater. Electron. 30 (2019) 12197–12203. X. Ji, C. Wang, W. Luo, G. Chen, S. Zhang, R. Tu, Q. Shen, J. Shi and L. Zhang, Effect of solution concentration on low-temperature synthesis of BCZT powders by sol-gel-hydrothermal method, J. Sol-Gel Sc. Tech., 94 (2020) 205-212.
[13] Q. Zhang, W. Cai, Q. Li, R. Gao, G. Chen, X. Deng, Z. Wang, X. Cao, C. Fu, *Enhanced piezoelectric response of (Ba,Ca)(Ti, Zr)O_3 ceramics by super large grain size and construction of phase boundary*, J. Alloys Compd. 794 (2019) 542–552.
[14] J.P. Praveen, T. Karthik, A.R. James, E. Chandrakala, S. Asthana, D. Das, Effect of poling process on piezoelectric properties of sol-gel derived BZT-BCT ceramics, J. Eur. Ceram. Soc. 35 (2015) 1785–1798.
[15] https://webofknowledge.com/ keywords used- Topic: "BCZT ceramics or (Ba0.85Ca0.15Zr0.1Ti0.9O3) ceramics" with Refine: "sol-gel".
[16] S. Nayak, B. Sahoo, T.K. Chakia, D. Khastgir, *Facile preparation of uniform barium titanate ($BaTiO_3$) multipods with high permittivity: impedance and temperature dependent dielectric behavior*, RSC Adv. 4 (2014) 1212–1224.
[17] C. Miot, E. Husson, C. Proust, R. Erre, J.P. Coutures, X-ray photoelectron spectroscopy characterization of barium titanate ceramics prepared by the citric route. Residual carbon study, J. Mater. Res. 12 (2011) 2388–2392.
[18] S. Kumar, V.S. Raju, T.R.N. Kutty, Investigations on the chemical states of sintered barium titanate by X-ray photoelectron spectroscopy, Appl. Surf. Sci. 206 (2003) 250.
[19] J.L. Jou, C.M. Lei, Y.W. Xu, W.C.V. Yeh, The higher energy components in Ti2p Xps spectrum of Ga doped barium titanate, Chin. J. Phys. 50 (2012) 926–931.
[20] B. Erdem, R.A. Hunsicker, G.W. Simmons, E.D. Sudol, V.L. Dimonie, M.S. ElAasser, *XPS and FTIR surface Characterization of TiO_2 particles Used in polymer encapsulation*, Langmuir 17 (2001) 2664.
[21] Q. Yu, D. Liu, R. Wang, Z. Feng, Z. Zuo, S. Qin, H. Liu, X. Xu, *The dielectric and photochromic properties of defect-rich $BaTiO_3$ microcrystallites synthesized from Ti_2O_3*, Mater. Sci. Eng., B 177 (2012) 639–644.
[22] T.S. Jeon, J.M. White, D.L. Kwong, *Thermal stability of ultrathin ZrO_2 films prepared by chemical vapor deposition on Si(100)*, Appl. Phys. Lett. 78 (2001) 368.

[23] C.C. Chusuei, D.W. Goodman, M.J. Van Stipdonk, D.R. Justes, E.A. Schweikert, Calcium phosphate phase identification using XPS and time-of-flight cluster SIMS, Anal. Chem. 71 (1999) 149–153.

[24] D.W. Boukhvalov, D.M. Korotin, A.V. Efremov, E.Z. Kurmaev, Ch Borchers, I. S. Zhidkov, D.V. Gunderov, R.Z. Valiev, N.V. Gavrilov, S.O. Cholakh, Modification of titanium and titanium dioxide surfaces by ion implantation: combined XPS and DFT study, Phys. Status Solidi B 252 (2015) 748–754.

[25] A.C. Larson, R.B. Von Dreele, Los Alamos National Laboratory Report LAUR 86 (2004) 748.

[26] B.H. Toby, EXPGUI, a graphical user interface for GSAS, J. Appl. Crystallogr. 34 (2001) 210.

[27] E.V. Ramana, F. Figueiras, A. Mahajan, D.M. Tobaldi, B.F.O. Costa, M.P.F. Graça, M.A. Valente, *Effect of Fe-doping on the structure and magnetoelectric properties of* $(Ba_{0.85}Ca_{0.15})(Ti_{0.9}Zr_{0.1})O_3$ *synthesized by a chemical route*, J. Mater. Chem. C 4 (2016) 1066–1079.

[28] K. Momma, F. Izumi, VESTA: a three-dimensional visualization system for electronic and structural analysis, J. Appl. Crystallogr. 41 (2008) 653–658.

[29] K. Brajesh, M. Abebe, R. Ranjan, *Structural transformations in morphotropic-phase-boundary composition of the lead-free piezoelectric system* $Ba(Ti_{0.8}Zr_{0.2})O_3-(Ba_{0.7}Ca_{0.3})TiO_3$, Phys. Rev. B 94 (2016) 104108.

[30] R.P.S.M. Lobo, N.D.S. Mohallem, R.L. Moreira, Grain-size effects on diffuse phase transitions of sol-gel prepared barium titanate ceramics, J. Am. Ceram. Soc. 78 (1995) 1343–1346.

[31] Y.N. Huang, X. Li, Y. Ding, Y.N. Wang, H.M. Shen, Z.F. Zhang, Domain freezing in potassium dihydrogen phosphate, triglycine sulfate, and CuAlZnNi, Phys. Rev. **B** 55 (1997) 16159.

[32] B.L. Cheng, T.W. Button, M. Gabbay, G. Fantozzi, M. Maglione, J. Am. Ceram. Soc. 88 (2005) 907–911.

[33] F. Jona, G. Shirane, Ferroelectric Crystals, Dover Publications, 1993.

[34] M. DiDomenico, S.H. Wemple, S.P.S. Porto, R.P. Bauman, *Raman Spectrum of single-domain* $BaTiO_3$, Phys. Rev. 174 (1968) 522.

[35] V. Buscaglia, S. Tripathi, V. Petkov, M. Dapiaggi, M. Deluca, A. Gajović, Y. Ren, *Average and local atomic-scale structure in* $BaZr_xTi_{1-x}O_3$ *(x= 0.10, 0.20, 0.40) ceramics by high-energy x-ray diffraction and Raman spectroscopy*, J. Phys. Condens. Matter 26 (2014), 065901.

[36] A. Dixit, S.B. Majumder, P.S. Dobal, R.S. Katiyar, A.S. Bhalla, Phase transition studies of sol–gel deposited barium zirconate titanate thin films, Thin Solid Films 447 (2004) 284.

[37] D.-Y. Lu, W. Cheng, X.-Y. Sun, Q.-L. Liu, D.-X. Lib, Z.-Y. Li, Abnormal Raman spectra in Er-doped BaTiO3 ceramics, J. Raman Spectrosc. 45 (2014) 963–970.

[38] J.D. Freire, R.S. Katiyar, *Lattice dynamics of crystals with tetragonal* $BaTiO_3$ *structure*, Phys. Rev. **B** 37 (1988) 2074.

[39] M. Deluca, C.A. Vasilescu, A.C. Ianculescu, D.C. Berger, C.E. Ciomaga, L. P. Curecheriu, L. Stoleriu, A. Gajovic, L. Mitoseriu, C. Galassi, *Investigation of the composition-dependent properties of* $BaTi_{1-x}Zr_xO_3$ *ceramics prepared by the modified Pechini method*, J. Eur. Ceram. Soc. 32 (2012) 3551.

[40] J. Kreisel, P. Bouvier, M. Maglione, B. Dkhil, A. Simon, *High-pressure Raman investigation of the Pb-free relaxor* $BaTi_{0.65}Zr_{0.35}O_3$, Phys. Rev. **B** 69 (2004), 092104.

[41] U.D. Venkateswaran, V.M. Naik, R. Naik, *High-pressure Raman studies of polycrystalline* $BaTiO_3$, Phys. Rev. **B** 58 (1998) 14256.

[42] L. Zhao, B.-P. Zhang, P.-F. Zhou, X.-K. Zhao, L.-F. Zhu, *Phase Structure and property Evaluation of (Ba,Ca)(Ti,Sn)*O_3 *Sintered with* Li_2CO_3 *Addition at low temperature*, J. Am. Ceram. Soc. 97 (2014) 2164.

[43] R. Comes, M. Lambert, A. Guinier, *The chain structure of* $BaTiO_3$ *and* $KNbO_3$, Solid State Commun. 6 (1968) 715–719.

[44] S. Miao, J. Pokorny, U.M. Pasha, O.P. Thakur, D.C. Sinclair, I.M. Reaney, *Polar order and diffuse scatter in* $Ba(Ti_{1-x}Zr_x)O_3$ *ceramics*, J. Appl. Phys. 106 (2009) 114111.

[45] Y.J. Jiang, L.Z. Zeng, R.P. Wang, Y. Zhu, Y.L. Liu, *Fundamental and second-order Raman Spectra of* $BaTiO_3$, J. Raman Spectrosc. 27 (1996) 31.

[46] M. Deluca, L. Stoleriu, L.P. Curecheriu, N. Horchidan, A. Carmen Ianculescu, C. Galassi, L. Mitoseriu, *High-field dielectric properties and Raman spectroscopic investigation of the ferroelectric-to-relaxor crossover in* $BaSn_xTi_{1-x}O_3$ *ceramics*, J. Appl. Phys. 111 (2012), 084102.

[47] A. Kumar, I. Rivera, R.S. Katiyar, *Investigation of local structure of lead-free relaxor* $Ba(Ti_{0.70}Sn_{0.30})O_3$ *by Raman spectroscopy*, J. Raman Spectrosc. 40 (2009) 459.

[48] D.I. Woodward, J. Knudsen, I.M. Reaney, *Review of crystal and domain structures in the* $PbZr_xTi_{1-x}O_3$ *solid solution*, Phys. Rev. **B** 72 (2005) 104110.

[49] E. Buixaderas, I. Gregora, S. Kamba, J. Petzelt, M. Kosec, Raman spectroscopy and effective dielectric function in PLZT x/40/60, J. Phys. Condens. Matter 20 (2008) 345229.

[50] D. Damjanovic, A. Biancoli, L. Batooli, A. Vahabzadeh, J. Trodahl, *Elastic, dielectric, and piezoelectric anomalies and Raman spectroscopy of* $0.5Ba(Ti_{0.8}Zr_{0.2})O_3$-$0.5(Ba_{0.7}Ca_{0.3})TiO_3$, Appl. Phys. Lett. 100 (2012) 192907.

[51] D.M. Smyth, The Defect Chemistry of Metal Oxides, Oxford University Press, 2000.

[52] A. Mahmoud, A. Erba, Kh E. El-Kelany, M. Rérat, R. Orlando, Low-temperature phase of BaTiO: piezoelectric, dielectric, elastic, and photoelastic properties from ab initio simulations, Phys. Rev. **B** 89 (2014), 045103.

[53] R.A. Evarestov, A.V. Bandura, First-principles calculations on the four phases of BaTiO3, J. Comput. Chem. 33 (2012) 1123–1130.

[54] L. Zhang, W. Gao, Y. Fang, S. Dai, Photoluminescence spectroscopy technology to probe phase transition process of Ba0.95Eu0.05TiO3, Exp. Tech. 40 (2016) 603–607.

[55] Y. Lou, Y. Chen, C. Liu, P. Chen, R. Jia, X. Liu, L. Yang, J. Li, N. Dai, Temperature induced modulation of near-infrared photoluminescence in BaTiO3: Er, J. Lumin. 223 (2020) 117220.

[56] H. Bae, K.T. Lee, Effect of tetragonal to cubic phase transition on the upconversion luminescence properties of A/B site erbium-doped perovskite BaTiO3, RSC Adv. 9 (2019) 2451.

[57] P.P. Sukul, K. Kumar, H.C. Swart, Photoluminescence spectroscopy of Eu3+: an economical technique for the detection of crystal phase transformation in PbZr0.53Ti0.47O3 ceramics, OSA Continuum 1 (2018) 971–980.

[58] V.S. Yalishev, R.A. Ganeev, A.S. Alnaser, S.U. Yuldashev, *Critical points in photoluminescence spectra and their relation with phase transition in Nb-doped* $SrTiO_3$, Appl. Phys. A126 (2020) 483.

[59] R.L. Milot, G.E. Eperon, H.J. Snaith, M.B. Johnston, L.M. Herz, Temperature-dependent charge-carrier dynamics in CH3NH3PbI3 perovskite thin films, Adv. Funct. Mater. 25 (2015) 6218–6227. S. Thomson, Observing Phase Transitions in a Halide Perovskite UsingTemperature Dependent Photoluminescence Spectroscopy , Technical Report, P45 (2018).

[60] S.A. Shojaee, T.A. Harriman, G.S. Han, J.-K. Lee, D.A. Lucca, Substrate effects on photoluminescence and low temperature phase transition of methylammonium lead iodide hybrid perovskite thin films, Appl. Phys. Lett. 111 (2017), 023902.

[61] R. Fulati, P. Dai, *The phase Transition and photoluminescence Properties of* $(Ca_{9-x}Sr_x)Mg_{1.5}(PO_4)_7:Eu^{2+}$ *solid-solution phosphors*, ECS J. Solid State Sc. Tech. 10 (2021), 036005.

[62] Q. Sun, Q. Gu, K. Zhu, R. Jin, J. Liu, J. Wang, J. Qiu, Crystalline structure, defect chemistry and room temperature colossal permittivity of Nd-doped barium titanate, Sci. Rep. 7 (2017) 42274.

[63] L.S. Cavalcante, M.F.C. Gurgel, A.Z. Simões, E. Longo, J.A. Varela, M.R. Joya, P. S. Pizani, Intense visible photoluminescence in Ba(Zr0.25Ti0.75)O3 thin films, Appl. Phys. Lett. 90 (2007), 011901.

[64] M.L. Moreira, M.F.C. Gurgel, G.P. Mambrini, E.R. Leite, P.S. Pizani, J.A. Varela, E. Longo, Photoluminescence of barium titanate and barium zirconate in multilayer disordered thin films at room temperature, J. Phys. Chem. A112 (2008) 8938–8942.

[65] J. Yu, J. Sun, J. Chu, D. Tang, *Light-emission properties in nanocrystalline* $BaTiO_3$, Appl. Phys. Lett. 77 (2000) 2807.

[66] M.L. Crespillo, J.T. Graham, F.A. López, Y. Zhang, W.J. Weber, Recent advances on carrier and exciton self-trapping in strontium titanate: understanding the luminescence emissions, Crystals 9 (2019) 95.

[67] S.G. Lu, Z.K. Xu, H. Chen, C.L. Mak, K.H. Wong, K.F. Li, K.W. Cheah, J. Time-resolved photoluminescence of barium titanate ultrafine powders, Appl. Phys. 99 (2006), 064103-1-4.

[68] A.E. Souza, G.T.A. Santos, B.C. Barra, W.D. Macedo Jr., S.R. Teixeira, C.M. Santos, A.M.O.R. Senos, L. Amaral, E. Longo, Photoluminescence of SrTiO3: influence of particle size and morphology, Cryst. Growth Des. 12 (2012) 5671–5679.

[69] N.N. Hasbullah, S.K. Chen, K.B. Tan, Z.A. Talib, J.Y.C. Liew, O.J. Lee, *Photoluminescence activity of* $BaTiO_3$ *nanocubes via facile hydrothermal synthesis*, J. Mater. Sci. Mater. Electron. 30 (2019) 5149–5157.

[70] W.A. Saidi, S. Poncé, B. Monserrat, Temperature dependence of the energy levels of methylammonium lead iodide perovskite from first-principles, J. Phys. Chem. Lett. 7 (2016) 5247–5252.

[71] A. Amat, E. Mosconi, E. Ronca, C. Quarti, P. Umari, M.K. Nazeeruddin, M. Grätzel, F. De Angelis, Cation-induced band-gap tuning in organohalide perovskites: interplay of spin–orbit coupling and octahedra tilting, Nano Lett. 14 (2014) 3608–3616.

[72] D. Gobeljic, V.V. Shvartsman, K. Wang, F. Yao, J.-F. Li, W. Jo, J. Rödel, D. C. Lupascu, *Temperature dependence of the local piezoresponse in (K,Na)*NbO_3*-based ceramics with large electromechanical strain*, J. Appl. Phys. 116 (2014), 066811.

[73] C. Ma, X. Tan, E. Dul'Kin, M. Roth, *Domain structure-dielectric property relationship in lead-free* $(1-x)(Bi_{1/2}Na_{1/2})TiO_3$-$xBaTiO_3$ *ceramics*, J. Appl. Phys. 108 (2010) 104105.

[74] J. Gao, Y. Hao, S. Ren, T. Kimoto, M. Fang, H. Li, Y. Wang, L. Zhong, S. Li, X. Ren, *Large piezoelectricity in Pb-free* $0.96(K_{0.5}Na_{0.5})_{0.95}Li_{0.05}Nb_{0.93}Sb_{0.07}O_3-0.04BaZrO_3$ *ceramic: a perspective from microstructure*, J. Appl. Phys. 117 (2015), 084106.

[75] J.F. Chou, M.H. Lin, H.Y. Lu, Ferroelectric domains in pressureless-sintered barium titanate, Acta Mater. 48 (2000) 3569.

[76] S. Shao, J. Zhang, Z. Zhang, P. Zheng, M. Zhao, J. Li, C. Wang, *High piezoelectric properties and domain configuration in* $BaTiO_3$ *ceramics obtained through solid-state reaction route*, J. Phys. D Appl. Phys. 42 (2009) 189801.

[77] G. Arlt, Twinning in ferroelectric and ferroelastic ceramics: stress relief, J. Mater. Sci. 25 (1990) 2655.

[78] N. Horchidan, A.C. Ianculescu, C.A. Vasilescu, M. Deluca, V. Musteata, H. Ursic, R. Frunza, B. Malic, L. Mitoseriu, *Multiscale study of ferroelectric–relaxor crossover in* $BaSn_xTi_{1-x}O_3$ *ceramics*, J. Eur. Ceram. Soc. 34 (2014) 3661.

[79] V. Likodimos, X.K. Orlik, L. Pardi, M. Labardi, M. Allegrini, Dynamical studies of the ferroelectric domain structure in triglycine sulfate by voltage-modulated scanning force microscopy, J. Appl. Phys. 87 (2000) 443.

[80] S.V. Kalinin, D.A. Bonnell, *Temperature dependence of polarization and charge dynamics on the* $BaTiO_3(100)$ *surface by scanning probe microscopy*, Appl. Phys. Lett. 78 (2001) 1116.

[81] V.V. Shvartman, A.L. Kholkin, *Polar structures of* $PbMg_{1/3}Nb_{2/3}O_3$-$PbTiO_3$ *relaxors: piezoresponse force microscopy approach*, J. Adv. Dielect. 2 (2012) 1241003.

[82] H.Y. Lee, K. Wang, F.Z. Yao, W. Sun, Z. Zhou, M.H. Zhang, X. Li, H. Luo, J.S. Lee, J. F. Li, *Identifying phase transition behavior in* $Bi_{1/2}Na_{1/2}TiO_3$-$BaTiO_3$ *single crystals by piezoresponse force microscopy*, J. Appl. Phys. 121 (2017) 174103.